

# Optimal Image Reconstruction in Radio Interferometry

E. C. Sutton

*Department of Astronomy, University of Illinois, 1002 W. Green St., Urbana, IL 61801*

B. D. Wandelt

*Departments of Physics and Astronomy, University of Illinois, 1110 W. Green St., Urbana, IL 61801*

`sutton@astro.uiuc.edu, bwandelt@uiuc.edu`

## ABSTRACT

We introduce a method for analyzing radio interferometry data which produces maps which are optimal in the Bayesian sense of maximum posterior probability density, given certain prior assumptions. It is similar to maximum entropy techniques, but with an exact accounting of the multiplicity instead of the usual approximation involving Stirling's formula. It also incorporates an Occam factor, automatically limiting the effective amount of detail in the map to that justified by the data. We use Gibbs sampling to determine, to any desired degree of accuracy, the multi-dimensional posterior density distribution. From this we can construct a mean posterior map and other measures of the posterior density, including confidence limits on any well-defined function of the posterior map.

*Subject headings:* methods: data analysis—methods: statistical—techniques: image processing—techniques: interferometric

## 1. INTRODUCTION

A radio interferometer samples the Fourier transform of the sky brightness distribution. This statement oversimplifies the situation (Thompson, Moran, & Swenson 2001), but is sufficient to illustrate the problem of reconstructing images of the radio sky. The brightness distribution  $I(\xi, \eta)$  is the inverse Fourier transform of the visibility function  $V(u, v)$ ,

$$I(\xi, \eta) = V(u, v).$$

Here  $\xi$  and  $\eta$  are directional cosines in the directions of increasing right ascension and declination, respectively, with respect to some phase center. The spatial frequency coordinates

$u$  and  $v$  are components of the projected baseline divided by the wavelength, conjugate to  $\xi$  and  $\eta$ , respectively. Since  $V(u, v)$  is of necessity incompletely sampled, the intensity distribution  $I(\xi, \eta)$  cannot be recovered uniquely by the inverse Fourier transform of  $V(u, v)$ . Instead, one initially can recover what is known as the principal solution, the inverse Fourier transform of the visibility times the sampling function. This results in a brightness distribution (the dirty map) consisting of  $I(\xi, \eta)$  convolved by the inverse Fourier transform of the sampling function (the dirty beam). Depending on the  $u - v$  sampling, the dirty beam will contain artifacts such as grating rings and sidelobes, which can be troublesome. The problem then is to recover a better view of the radio sky than this principal solution. We use the term principal solution whenever the visibility is set to zero at unsampled points, regardless of any weighting applied to the sampled data.

The procedure CLEAN, used to address this problem, was first described by Högbom (1974). The technique may be visualized by considering the sky as containing a finite assembly of point sources. The algorithm sequentially identifies the strongest source, removes the beam pattern produced by such a source, and iterates until the noise level is reached. The implicit prior is that the sky brightness distribution is zero over most of the image. Subsequently, attention was given to techniques variously known as phase closure, self calibration, and hybrid mapping (Readhead & Wilkinson 1978; Cornwell & Wilkinson 1981; Schwab & Cotton 1983), techniques which were effective at removing phase and amplitude instabilities in interferometry data. It is usually assumed that the complex gain for a given baseline can be factored into complex antenna-based gains,

$$\tilde{G}_{\alpha\beta} = \tilde{g}_\alpha \tilde{g}_\beta^* .$$

The problem is more complex if the passbands differ enough so that such factorization is not possible. CLEAN, as described above, exhibits a striping instability in regions of extended emission. Cornwell (1983) and Steer, Dewdney, & Ito (1984) addressed this problem, although in different fashions. The situation through 1984 was summarized by Pearson & Readhead (1984). Brinks & Shane (1984) and Wakker & Schwarz (1988) subsequently introduced a multi-scale approach to CLEAN.

Other work concentrated on the problem of the missing "zero-spacing" data, which produces bowls of negative emission (depressions) around strong sources. Since an interferometer cannot observe with zero baseline, the principal solution map always contains zero net flux. A solution is to augment interferometric data with either total-power or mapping data from large single-dish telescopes. This problem was addressed by Bajaja & van Albada (1979); Ekers & Rots (1979); Vogel et al. (1984); Mundy et al. (1988); Cornwell (1988). This topic encroaches upon other deconvolution methods, such as maximum entropy, and is discussed below. It also is related to mosaic mapping (Sault, Staveley-Smith, & Brouw 1996),

also discussed below.

CLEAN has become the best established method of reducing radio interferometer data, despite its proclivity to reproduce point sources well while poorly reproducing regions of extended emission. We believe this is mostly a matter of habit among astronomers, who have become attached to the intuitive nature of CLEAN. However, it contains some troubling features including its non-linear nature, the implicit emptiness prior, and a number of *ad hoc* choices such as the loop gain, the restoring beam, and the stopping criteria. A non-linearity cannot be avoided if an improved map is to be obtained. The first and the third of these *ad hoc* choices (to use the splendid coinage of Jaynes (1982, 2003)) seem to have little practical consequence, although the *ad hoc* restoring beam sometimes prevents observers from seeing the full resolution (superresolution) justified by high signal-to-noise data.

Even in the original work of Högbom (1974), the main advantage of CLEAN was described as the ease of computation. Högbom seemed to anticipate the advantages of maximum entropy algorithms, even using language remarkably Bayesian in character. Computing power may have been a sufficient justification in favor of CLEAN in 1984. But lack thereof is certainly insufficient justification for current and future generations of radio interferometers such as CARMA and ALMA.

The maximum entropy method (MEM) introduced by Ables (1974) was developed for image restoration by Gull & Daniell (1978); Bryan & Skilling (1980); Gull & Skilling (1984a); Cornwell & Evans (1985) as an alternative to CLEAN. The technique also has found great success in crystallography, geophysics, tomography, and a variety of other applications. A review of MEM in the context of image restoration in astronomy was given by Narayan & Nityananda (1986). The basic idea of MEM is to provide an image which has the smallest amount of structure, the maximum entropy, while remaining consistent with the observed visibilities within observational uncertainties. Much of this work used the configurational entropy as the appropriate measure of entropy. We write this as

$$S = - \sum_i \frac{I_i}{I_t} \ln \frac{I_i}{I_t},$$

where the summation is over all pixels and

$$I_t = \sum_i I_i.$$

The normalization with  $I_t$  keeps the argument of the logarithm dimensionless. In this formulation the entropy has natural units, known variously as "nits", "nats", or "nepers" (the units would be "bits" if  $\log_2$  had been used). There is no multiplicative constant, as this would simply correspond to a change of units and a change in the base for logarithms and

exponentiation. This is important in our analysis. We do not include the concept of default image models, since we believe they would be difficult to specify reliably in astronomical imaging.

The penalty function is taken to be

$$\frac{\chi^2}{2} - \lambda S$$

where  $\lambda$  is a Lagrange multiplier, and the penalty function is to be minimized, subject to some constraint. The term  $\lambda$  is often viewed as a control parameter, adjusting the degree of smoothness imposed on the solution. From an information-theoretic point of view and following Jaynes (1982), we show below that this constrained optimization problem may be viewed equivalently as an unconstrained Bayesian maximization. This assumes that the desired result is the map with maximum *a posteriori* probability density. We also show that it is possible to obtain important additional information about the posterior probability density distribution. The value of  $\lambda$  should be determined by the data. However, if the magnitude of the errors in the experimental data are not known well, then the scaling of  $\chi^2$  is unknown and a Lagrange multiplier will be needed. The total flux in the map is  $I_t$  times the solid angle per pixel. Some approaches include an additional Lagrange multiplier for the total flux. If the total flux is known from one or more single-dish measurements, they may be included as terms in  $\chi^2$ . If not, it is hard to see how to justify such a term.

Mundy et al. (1988) and Cornwell (1988) extended the MEM approach to include joint deconvolution of single-dish and interferometer data. Our work here is a continuation along this general line, merging such considerations with the maximum entropy approach of Gull & Daniell (1978) into a proper Bayesian framework. It also allows for a simple inclusion of mosaic data.

## 2. BAYESIAN ANALYSIS

From the beginning of this development, terms like "prior" and "a priori information" have appeared frequently in the literature without, however, many attempts at formal Bayesian analysis. The MEM discussions of Gull & Daniell (1978) and Jaynes (1982) have come closest. Bayes theorem may be derived from the product rule,

$$P(AB|C) = P(A|BC) P(B|C)$$

$$P(AB|C) = P(B|AC) P(A|C).$$

$P(AB|C)$  stands for the conditional probability of A and B, given C, etc. Combining these two equations we get Bayes equation,

$$P(H|DI) = P(H|I) \frac{L(D|HI)}{P(D|I)},$$

where we substitute H (standing for hypothesis) for A, D (standing for data) for B, and I (standing for information) for C. The information I represents our combined knowledge about such things as beam patterns, measurement errors, etc. Our various hypotheses are maps, and we wish to find maps with high probability.

The left-hand side of the equation is referred to as the posterior. The first term on the right-hand side is referred to as the prior. The numerator of the second term is the likelihood, indicated by the symbol L, and the denominator (the "evidence") is a normalization factor which sometimes may be ignored. The interpretation of Bayes theorem is that the posterior probability of any hypothesis H is given by the product of one's prior knowledge of that hypothesis times the likelihood that the hypothesis would have produced the observed data (suitably normalized).

## 2.1. Likelihoods

The likelihood of the data, given the model and the information, can be factored into multiple terms if the data are independent. This is nothing more than what one does in calculating  $\chi^2$ , where each datum is represented by a multiplicative term in the likelihood and therefore an additive term in the logarithm of the likelihood ( $\chi^2/2$ ). Here we factor the likelihood into two terms:  $L_{int}$  for the observed set of interferometric data (visibilities) and  $L_{sd}$  for any image-domain measurements obtained from single-dish pointings or mappings.

$$L(\{Data\}|I(\xi, \eta) I) = L_{sd}(\{T_k\}|I(\xi, \eta) I) \times L_{int}(\{V_k\}|I(\xi, \eta) I).$$

The single-dish likelihood is the product, over various pointings of the telescope towards celestial offset coordinates  $\{\xi_k, \eta_k\}$ , of the likelihood of each measured antenna temperature in  $\{T_k\}$ . For simplicity we assume the single dish beam pattern to be symmetrical and Gaussian (a property we also assume for the individual telescope beams in the interferometers). Generalization to more complex patterns is straightforward (Armitage & Wandelt 2004). We describe the antenna pattern in terms of the effective collecting area,  $A_{eff}$ , as a function of angles with respect to the telescope pointing direction. For a given map  $I(\xi, \eta)$ , the expected antenna temperature is

$$T'_k(\xi_k, \eta_k) = \frac{1}{2k_b} \int \int I(\xi, \eta) A_{eff}(\xi - \xi_k, \eta - \eta_k) d\xi d\eta.$$

The symbol  $k_b$  represents Boltzmann’s constant. We assume additive, independent Gaussian noise with probability distribution

$$P(N) = \frac{1}{\sqrt{2\pi\sigma_k^2}} e^{-N^2/2\sigma_k^2}$$

$$\sigma_k = \frac{K T_{sys}}{\sqrt{\Delta\nu \tau}},$$

where  $K$  is a constant of order unity that depends on the method of observation (e.g. beam switching),  $T_{sys}$  is the system noise temperature,  $\Delta\nu$  is the bandwidth, and  $\tau$  is the integration time. The noise  $\sigma_k$  may vary between measurements. The likelihood of the observed  $\{T_k\}$  is

$$L_{sd}(\{T_k\} | I(\xi, \eta) I) = \prod_{k=1}^{N_{sd}} \frac{1}{\sqrt{2\pi\sigma_k^2}} e^{-(T_k - T'_k)^2/2\sigma_k^2}$$

and the log likelihood (ignoring constant terms) is

$$\ln L_{sd}(\{T_k\} | I(\xi, \eta) I) = -\frac{1}{2} \sum_{k=1}^{N_{sd}} \frac{(T_k - T'_k)^2}{\sigma_k^2}.$$

The interferometric likelihood is the product, over the various visibility measurements in  $\{\tilde{V}_k\}$ , of the likelihood of each such visibility at spatial frequencies  $\{u_k, v_k, w_k\}$ , given a map  $I(\xi, \eta)$ . We assume the bandwidth pattern to be unity, as it would be for negligible bandwidth, or to be incorporated into the antenna pattern. The expected visibility is

$$\tilde{V}'_k(u_k, v_k, w_k) = \iint P_N(\xi, \eta) I(\xi, \eta) \frac{\exp\{-i2\pi[\xi u_k + \eta v_k + w_k(\sqrt{1 - \xi^2 - \eta^2} - 1)]\}}{\sqrt{1 - \xi^2 - \eta^2}} d\xi d\eta,$$

where  $P_N$  is the normalized power pattern of an individual telescope, given by

$$P_N(\xi, \eta) = A_{eff}(\xi, \eta) / A_{eff}(0, 0).$$

Since the interferometric antennas are not generally the same as the single dish antennas, the symbol  $A_{eff}$  can take on different meanings. We believe the meaning will be clear, depending on the context. If the telescopes of an interferometric pair have different power patterns, the geometric mean of their power patterns should be used,

$$P_N = \sqrt{P_\alpha P_\beta}.$$

Note the use of the exact kernel in the transform integral, rather than the Fourier kernel, which is only approximate. Here we assume additive, independent, bivariate Gaussian noise with distribution

$$P(\tilde{N}) = \frac{1}{2\pi\sigma_k^2} e^{-(Re\tilde{N})^2/2\sigma_k^2} e^{-(Im\tilde{N})^2/2\sigma_k^2}$$

where

$$\sigma_k = \frac{2k_b T_{sys}}{A_{eff} \eta_Q} \frac{1}{\sqrt{\Delta\nu \tau}}.$$

The quantization efficiency factor  $\eta_Q = 0.881$  for 2 bit (4 level) quantization at the Nyquist rate (Thompson, Moran, & Swenson 2001). The system temperature is the geometric mean of the system temperatures of the pair of telescopes involved in the observation,

$$T_{sys} = \sqrt{T_\alpha T_\beta}.$$

The likelihood of the observed  $\{\tilde{V}_k\}$  is

$$L_{int}(\{\tilde{V}_k\} | I(\xi, \eta) I) = \prod_{k=1}^{N_{int}} \frac{1}{2\pi\sigma_k^2} e^{-|\tilde{V}_k - \tilde{V}'_k|^2/2\sigma_k^2}$$

and the log likelihood (ignoring constant terms) is

$$\ln L_{int}(\{\tilde{V}_k\} | I(\xi, \eta) I) = -\frac{1}{2} \sum_{k=1}^{N_{int}} \frac{|\tilde{V}_k - \tilde{V}'_k|^2}{\sigma_k^2}.$$

For mosaic mapping, all that is necessary is to incorporate pointing offsets into the definition of  $\tilde{V}'_k$ , just as was done for  $\tilde{T}'_k$ .

## 2.2. Matrix Formulation

For many purposes the most convenient method of calculating likelihoods is to formulate the problem as a matrix multiplication

$$D = MI + \epsilon.$$

The image  $I$  of the sky is represented by a vector enumerating the values of the various pixels, with some specified ordering of the  $n$  pixels. The measurement matrix  $M$  converts the image into a variety of measurable quantities  $D$  (data), which may include both visibility data and single-dish data. Noise  $\epsilon$ , assumed to be Gaussian with zero mean, is added in the measurement process. In the absence of other information about the sources of noise, the choice of a Gaussian is least informative. We do not attempt to invert this equation. Rather, if the measurement matrix is known exactly and the statistical properties of the noise are known exactly, one can use this directly to calculate the log likelihood

$$\ln L = -\frac{1}{2} \sum_{k=1}^{N_{data}} \frac{|D_k - M_{kj} I_j|^2}{\sigma_k^2}.$$

This formulation is general enough to include single-dish data, interferometric data, and mosaic data. The measurement matrix may contain some number of unknown parameters,  $M(\alpha, \beta, \gamma, \dots)$ , whose distributions we also seek to discover.

### 2.3. Priors

We seek a pixel-based description of the intensity distribution. The pixels are square, of equal size, and uniformly distributed. The region likely to contain relevant information is circular and approximately the size of the FWHM of the main telescope beam. The region of support of the intensity distribution (the region mapped) should have a diameter approximately twice that of the primary telescope beam. If there is a strong source well out into the tails of the primary beam, the support region may be enlarged as necessary. For a heterogeneous array, the support should be twice the geometric mean of the main beams of the two smallest telescopes. The pixel size should be chosen to allow for some degree of superresolution, with several pixels across the synthesized beam.

What prior information is available? The intensity is real, which means that the visibilities must be Hermitian (ignoring the  $w_k$  terms in the transform kernel). This fact is not explicitly required here, and each observed visibility may be considered only once, at its conventional  $u, v$  location. The intensity in each pixel is also non-negative. A positive, additive distribution of this sort should be treated with an entropy prior (Sivia 1996). This is done below, although in a manner somewhat different than the conventional approach.

Following Jaynes (1982) and Gull & Daniell (1978), we consider the intensity distribution as if it were constructed by the conventional "team of monkeys" throwing  $\lambda$  "elements of luminance" among the various pixels. However, unlike some authors we do not take the limit  $\lambda \rightarrow \infty$  nor necessarily the case of  $\lambda$  much greater than the number of pixels. Therefore we retain the key feature of brightness quantization (Jaynes 1982; Gull & Daniell 1978). The number of such "elements of luminance" and the level of brightness quantization ( $q$ ) will be determined by Bayes theorem. No physical quantization is implied; these are not photons.

For distributing  $\lambda$  elements among  $n$  pixels, the multiplicity of some particular distribution  $\{N_i!\}$  is given by

$$W = \frac{\lambda!}{N_1! N_2! \cdots N_n!}.$$

At this point most authors take the limit  $\lambda \rightarrow \infty$  and approximate  $\lambda!$  and *all* of the  $\{N_i!\}$  using the leading term in Stirling's formula, yielding

$$\begin{aligned} \ln W &= \frac{1-n}{2} \ln 2\pi + \frac{\ln \lambda}{2} - \frac{1}{2} \sum_i \ln N_i - \lambda \sum_i \frac{I_i}{I_t} \ln \frac{I_i}{I_t} \\ &\approx \lambda S, \end{aligned}$$

where  $S$  is the logarithmic form of the configurational entropy discussed in section 1. We will not use Stirling's formula, since many of the  $\{N_i!\}$  may be of order unity. For this reason we prefer to refer to ours as a *multiplicity* prior, to differentiate it from the conventional *entropy*

prior. Also note that in the  $\lambda \rightarrow \infty$  limit, the posterior density becomes proportional to  $e^{\lambda S - \chi^2/2}$  (Jaynes 2003). This results in a perfectly flat distribution (the prior overwhelms the likelihood), further illustrating that the use of Stirling’s formula is inappropriate in this context. Instead,  $\lambda$  should be treated as a finite term whose value is to be determined by Bayes theorem.

Since there are  $n^\lambda$  possible configurations, the properly normalized prior distribution is

$$p(\{N_i!\}) = \frac{W}{n^\lambda}.$$

As  $\lambda$  gets larger, the prior probability drops due to the normalization factor of  $n^\lambda$  in the denominator. This is the automatic application of Occam’s razor which occurs in all Bayesian calculations. Any set of data allows only a certain amount of detail in the posterior, corresponding to the information content of the data.

We take a joint prior on the quantization level ( $q$ ), the number of luminance elements ( $\lambda$ ), and their distribution ( $\{N_i\}$ ) and factor it as

$$p(\{N_i\}\lambda q|I) = p(\lambda q|I) p(\{N_i\}|\lambda qI).$$

The product  $\lambda q$  is a scale parameter and should be given a Jeffreys prior. It also represents the total flux in the map. In our reconstructions the total flux is generally constant, with  $\lambda$  varying approximately as  $q^{-1}$ . So for simplicity we consider the term  $p(\lambda q|I)$  to be constant. The use of a Jeffreys prior would make little difference. The logarithm of the map prior (neglecting constants) is

$$\ln p(\{N_i\}\lambda q|I) = \ln W - \lambda \ln n.$$

Therefore the logarithm of the posterior is  $\ln W - \lambda \ln n - \chi^2/2$ . According to Bayesian logic, one then should vary  $\lambda$ ,  $q$ , and the  $\{N_i\}$  to explore the posterior density. The posterior of the image is then obtained by marginalizing  $q$  and  $\lambda$ .

For a clear and interesting discussion of the question of the appropriate  $\lambda$ , see chapters 5 and 6 of Sivia (1996). We believe that our treatment of  $\lambda$  meets the requirements of Narayan & Nityananda (1986), who described this as an unsolved problem. Our treatment of  $\lambda$  differs from and is preferable to that of Gull & Daniell (1978), who chose  $\lambda$  so that  $\chi^2 = N_{data}$ , a reasonable but *ad hoc* choice. Finally, take note of the cautions given by Jaynes (2003), who warns about the transition from the discrete to the continuum case and paradoxes that can arise with the latter.

Specification of prior information is the trickiest part of Bayesian analysis. Failure of the Bayesian technique is almost always due to the failure to incorporate all relevant prior information or to the incorporation of incorrect prior information. We have spoken of

the positive-definite nature of the intensity. Here we have to be careful. Bracewell (1979) pointed out that "a lot of entropy lies around the low brightness fringe so the choice of the boundary [zero] is not a trifle." Narayan & Nityananda (1986) commented further on this point. What is generally referred to as "zero" in radio interferometric maps is not necessarily the true zero in intensity. Neither interferometric measurements nor position-switched single-dish measurements are sensitive to a spatially uniform component of the emission. So in continuum maps the true zero of intensity may lie somewhat below the zero of the map. In spectroscopic mode the problem is further complicated by the convention of making maps from "continuum-subtracted" data. Since spectral lines and continuum often have different spatial distributions, the issue of the true zero of the intensity – which relates to their sum – intimately links the continuum and the spectral line maps. We defer the treatment of spectral line mapping to a later time, treating here only the continuum case.

## 2.4. Implementation

We first perform a multi-dimensional maximization of the posterior density. Because of the brightness quantization, this is a problem in combinatorial optimization. Such problems are notoriously difficult. Our parameter space has potentially tens of thousands of dimensions. This precludes an exhaustive search for the global maximum of the posterior density. Instead we may attempt to find one or more good (high probability) local maxima and a statistically valid sampling of the posterior probability density.

We make an initial guess for the quantization level,  $q$ . Then we pick an initial intensity distribution. This may be as simple as an empty (zero) map. But under many circumstances it may be advantageous to start from a better first approximation, such as a component map produced by CLEAN or a maximum entropy map. In such cases the map must then be quantized by taking the pixel values, dividing by  $q$ , the flux per quantum, and rounding to an integer value.

The posterior is then maximized by performing a grid search using the algorithm described in Appendix A. The quantization level is then also varied, possibly over a wide range, to find a region in  $q$  over which the posterior is maximized. The general appearance of the posterior map remains similar over a large range of brightness quantizations.

This technique is computationally intensive in terms of both memory requirements and calculational speed. The work described here has been performed on a single 1 GHz processor of a workstation-class machine with 1 GBy of memory. However, this type of problem may be highly parallelized with both computational and memory requirements spread over a number

of processors. Savings in storage and computation may be achieved by making careful use of the Hermitian nature of the transform kernel. For the case of finite values of  $w_k$ , the kernel may be factored into two terms, one of which is Hermitian. The other is non-Hermitian but symmetric.

## 2.5. Joint Densities

Complete information about the image is contained not just in the optimum posterior map (the mode of the probability density), but in the multi-dimensional joint probability density of the quantization level  $q$ , and the occupation numbers of all the pixels. Hobson & McLachlan (2003) discuss in a variety of astrophysical contexts the advantages of considering the complete posterior distribution.

We use a variant of Gibbs sampling to numerically estimate the joint posterior density. The Gibbs sampler is a particular example of the Markov-chain Monte Carlo method. Its advantage is that it splits a multi-dimensional sampling problem into a set of lower-dimensional sampling problems. In our case, the univariate conditional densities for individual pixels are readily calculable from the value of  $q$  and the values of all the other pixels. These distributions are discrete, and only a small number of states have non-negligible probabilities. From an initial state  $\{N_i^0\}, q^0$  one obtains an updated state  $\{N_i^1\}, q^1$  by a scan through the pixels, successively updating the  $\{N_i\}$  by random draws from

$$\begin{aligned} p(N_1^1 | N_2^0, N_3^0, \dots, N_n^0, q^0) \\ p(N_2^1 | N_1^1, N_3^0, \dots, N_n^0, q^0) \\ \dots \\ p(N_n^1 | N_1^1, N_2^1, \dots, N_{n-1}^1, q^0). \end{aligned}$$

Next, it is necessary to consider the continuous variable  $q$ , for which the conditional density is not readily available. This variable is updated with a Metropolis-Hastings step using draws from a Gaussian proposal density. The move to the updated value  $q^1$  is accepted with probability  $\min(1, r)$  where

$$r = \frac{p(q^1 | \{N_i^1\})}{p(q^0 | \{N_i^1\})}.$$

The procedure is then repeated to obtain successive samples  $\{N_i^2\}, q^2, \{N_i^3\}, q^3, \dots$

The Gibbs sampler requires some time to burn-in, that is, to achieve a stationary distribution. For this reason some initial number of samples need to be discarded. One may run a number of Gibbs chains simultaneously, usually from different starting points, to test

convergence and the coverage of parameter space. Successive samples in a Gibbs chain are somewhat correlated, so it is common to thin the chain by discarding samples less than a correlation length apart. The practicalities of these issues in the current context will be discussed below.

## 2.6. Marginalization

Maps can be made by this procedure from self-calibrated data. But logically, the complex antenna-based gains,  $\{\tilde{g}_\alpha\}$ , can and should be determined simultaneously along with the map. These gains are then treated as nuisance parameters and marginalized in order to obtain the optimum map. The least informative priors for  $\{\tilde{g}_\alpha\}$  are uniform in phase and Jeffreys  $1/|\tilde{g}_\alpha|$  priors in amplitude. If the original amplitude calibration is believed to be nearly correct, an amplitude prior distribution centered on  $|\tilde{g}_\alpha|=1$  may be substituted. But the width of such a distribution should be sufficient to encompass all realistic gain amplitude variations. This has the potential to provide a distinct improvement over current techniques in which the self-calibration step determines fixed values for the complex gains within some time interval. If such values are uncertain, treating them as known can lead to seriously degraded maps. However, treating them as unknown and uncertain parameters in the measurement matrix allows one to determine and then marginalize over their individual probability distributions. In the Bayesian context, this is the correct way to deal with such parameters. Other instrumental parameters may be treated in a similar manner.

## 2.7. Advantages

The above procedure requires no gridding, interpolation, or averaging of the visibility data, practices which have been shown by Briggs (1995) to cause problems in the CLEAN procedure. In Bayesian analysis such practices are obviously incorrect as they involve a loss or corruption of information. The procedure also does not require an *ad hoc* choice of weighting schemes, whether natural or uniform weighting, Briggs robust weighting (Briggs 1995), or otherwise. The Bayesian analysis automatically makes optimal use of each visibility measurement, in the information-theoretic sense, without requiring the user to make tradeoffs. These advantages, however, require considerably greater computational resources.

Since we avoid gridding and therefore do not use the fast Fourier transform (FFT), the measurement matrix may be set up exactly, including the  $w$  component of the interferometer baseline along the line of sight, at little additional cost. Visibilities then are no longer Fourier

transforms of the intensity distribution. Instead the transform kernel is

$$\frac{\exp\{-i2\pi[\xi u + \eta v + w(\sqrt{1 - \xi^2 - \eta^2} - 1)]\}}{\sqrt{1 - \xi^2 - \eta^2}}.$$

### 3. Numerical Results and Tests

Given the variety of situations that can arise in radio astronomy, no single example can prove the general superiority of one technique of data reduction over another. We believe that the arguments presented above show the theoretical advantages of our method. Here we present an example for the purpose of illustrating its operation and its practicality.

#### 3.1. Test Object

We simulate observations at a frequency of 100 GHz for a region of the sky containing 8 elliptical Gaussian components as shown in Table 1 and Figure 1a. The parameters were drawn from random distributions. The logarithms of the component fluxes were chosen from a distribution from 0.05 to 5 Jy. The component centers were chosen within a circle of radius 58 arcsec, representing the half-power beam of the BIMA telescopes at this frequency. Semi-major axes were chosen from a logarithmic distribution from 1 to 10 arcsec. The resulting peak surface brightnesses varied by over 2.5 orders of magnitude.

#### 3.2. Model Data

Artificial  $u, v$  data were generated by the Miriad task *uvgen* to simulate the process of observing with the BIMA B-array at 100 GHz. The observations were assumed to be taken over an hour angle range of  $-4$  to  $+4$  hours, with 2 minute integrations separated by 2 minute gaps. The center of the field of view was taken to be 30 degrees north declination, and the latitude was 40 degrees north. Minimum and maximum  $u, v$  distances were  $4.46 \text{ k}\lambda$  and  $78.00 \text{ k}\lambda$ , as shown by the  $u, v$  sampling pattern in Figure 2. Additive, independent Gaussian noise corresponding to fixed system temperatures of 120 K was included for each integration. A single continuum channel with bandwidth of 1000 MHz was taken. The effective area of the telescope was assumed to correspond to 150 Jy/K. No systematic, antenna gain or system temperature fluctuations were included. The resulting set of 5490 complex visibilities was then taken to be the data set for the observations, to be processed by the Bayesian algorithm.

Figure 1b shows a principal solution map for these observations, using natural weighting, to illustrate the level of sidelobe contamination present.

### 3.3. Pixels, Units, etc.

The effective resolution of the BIMA B array was of order 2 arcsec. To satisfy the sampling theorem we require a pixel size of

$$\Delta\xi = \Delta\eta < \frac{1}{2} \frac{\lambda}{B_{max}} \text{ rad} \approx 1.03 \times 10^5 \frac{\lambda}{B_{max}} \text{ arcsec} ,$$

where  $B_{max}$  is the maximum projected baseline length. So in this case we choose

$$\Delta\xi = \Delta\eta = 1 \text{ arcsec} .$$

The pixel solid angle  $\Omega_{pix} = \Delta\xi\Delta\eta = 2.35 \times 10^{-11} \text{ sr}$ . The diameter of the main beam is 115 arcsec. The support is twice this diameter, yielding a total of 41545 pixels. The unit of brightness is Jy per steradian. One may multiply by  $\Omega_{pix}$  to get Jy per pixel. The brightness is related to the usual radio astronomy Rayleigh-Jeans brightness temperature by the relation

$$T_b = \frac{\lambda^2}{2k_b} I(\xi, \eta) .$$

All integrals over the brightness distribution become sums over the pixels.

Ground-based single-dish measurements are usually made in a differential mapping mode. Therefore, any spatially uniform brightness is not measured. The same is true of interferometric measurements. However, as discussed above in section 2.3, the true zero of intensity should be taken into account. At millimeter wavelengths such a uniform background brightness distribution is present in the form of the cosmic microwave background (CMB). We require that the total intensity be positive definite, not the intensity relative to the CMB. Taking  $T_{CMB} = 2.726 \text{ K}$ , the brightness of the CMB is given by

$$T_b(\nu) = \frac{h\nu}{k_b} \frac{1}{e^{h\nu/k_b T_{CMB}} - 1} .$$

At 100 GHz this corresponds to a brightness temperature of 1.00 K and an intensity of  $7.2 \text{ mJy arcsec}^{-2}$ . The presence of the CMB is not currently taken into account.

### 3.4. Results

First the data were reduced using the *clean* and *maxen* (maximum entropy) tasks in Miriad. Since these methods have adjustable parameters, there is no unique answer for

either technique. But parameters were chosen that seemed appropriate for these test data (e.g. `robust=-1` in `invert` and `rms=0.001` Jy/beam in `maxen`). CLEAN produces both positive and negative artifacts, whereas MAXEN produces only positive artifacts. CLEAN has no knowledge of there being an absolute zero of intensity. MAXEN does, but has no knowledge of uniform background emission from the CMB.

We also used a non-negative least squares (NNLS) technique. Again, "non-negative" should refer to the true zero of intensity, although no information about uniform background emission has been included here. With 41545 pixels and 5490 complex visibility data such a map is underconstrained, but non-negativity is a strong regularizer. The underconstraint problem could be further ameliorated by removing pixels beyond the half-power beam radius (a more compact support) or by using fewer, larger pixels. Instead, we further regularize the NNLS solution by adding a multiplicity-like term. The gamma function may be used as an analytic replacement for the factorials in our earlier development. We refer to this technique as Gamma-regularized NNLS ( $\Gamma$ -NNLS). Further details on this regularizer are given in Appendix C. By this means we achieve a continuous (as opposed to discrete) multi-dimensional space in which the figure-of-merit is differentiable. This allows us to use a conjugate-gradient method of optimization. It must be emphasized that this technique itself is not Bayesian, although it has many close similarities with our Bayesian method.

The resulting maps are shown in Figure 3. The CLEAN map, made using the Clark (1980) algorithm, is shown in Figure 3a. Sources 2, 4, 5, 6, 7, and 8 are clearly present. The most compact sources (numbers 4 and 8) are spatially enlarged by the 2.56 x 2.07 arcsec restoring beam. The most extended source (number 2) is seen, but neither its size nor its flux are well reproduced by this technique. Peak residual artifacts (noise and sidelobes) in the CLEAN map are at the level of +0.0008 and -0.0009 Jy/pixel, near the level of the lowest contour. Source 1 may be marginally detected just below the lowest map contour shown. There is no evidence of source 3. Since sources away from the center of the map are attenuated by the primary beam, the CLEAN map has been reproduced in Figure 3b after division by the primary beam profile. Note the increased brightnesses of source 2 and 7, which are near the half power radius of the primary beam.

The MAXEN map is shown in Figure 3c. The strong compact sources 4 and 8 are well represented in size and shape and are fairly well represented in flux. Sources 5 and 6 are also clearly present. There are traces of sources 2 and 7, although both are in regions of strong sidelobe confusion (cf. Fig. 1b). There are no negative artifacts, and the largest positive artifact is +0.0017 Jy/pixel. The overall range of artificial structure in the map (positive to negative) is therefore the same as that of the CLEAN map. Maximum entropy maps exhibit a bias towards positive intensities. The source of this bias is a logarithmic singularity in the

derivative of the configurational entropy at zero brightness, as illustrated in Appendix C.

The  $\Gamma$ -NNLS map is shown in Figure 3d. The peak brightness on source 8 exceeds that of both the CLEAN and the MAXEN maps. Sources 4, 5, and 6 are also seen. All of these are well represented in size and shape. The extended sources 2 and 7 are present; their structures are reproduced better than in the MAXEN map and similar to the CLEAN map. The faint source 1 is clearly visible, and there are even suggestions of source 3. No negative artifacts are present, and the largest positive artifact is +0.0045 Jy/pixel, larger than for the overly smoothed MAXEN map in Figure 3c. However, values this large are seen only well outside of the primary beam, practically at the edges of the map. Recovered fluxes are discussed below.

The Bayesian algorithm was applied to the same data. There were no adjustable parameters. To improve the convergence speed, the map may be started with a reasonable first guess. We have seen best results starting from our  $\Gamma$ -NNLS map. The posterior varies with the level of quantization, which was scanned separately over a range from 0.001 to 0.025 Jy/pixel. The map was reoptimized at each quantization level. The dependences of  $\chi^2/2$ ,  $\ln W - \lambda \ln n_{pix}$ , and the posterior on the quantization level  $q$  are shown in Figure 4. Note that  $\lambda$  is approximately proportional to  $q^{-1}$ , as expected for fixed total flux. In this case the maximum posterior density occurs at a level of about 0.017 Jy/pixel, and 447 quanta are required to make the map. This map, often called a *maximum a posteriori* (MAP) estimator, is shown in Figure 5. We will refer to this as the posterior mode map. Since we cannot exhaustively search parameter space, we do not know that this mode is the true posterior maximum, only that it is the largest local maximum found in our search. It is likely that configuration space contains many nearly degenerate modes.

The minimum value of  $\chi^2/2$  in Figure 4 is 5520, which is close to the number of measurements (5490 complex visibilities, or 10,980 real data) and within the 68% confidence range of expected values for chi-squared. Given that we restrict ourselves to brightness quantized maps on 1 arcsec pixels with the posterior maximized at fixed quantization, one might not have expected such good agreement.

The Bayesian posterior mode map shows compact sources 4, 5, 6, and 8. The extended sources 2 and 7 are also clearly present, with distributions as smooth as might be expected for a coarsely quantized map. Occam’s razor discriminates against finer quantization. But intermediate brightnesses (for example, values between 0 and 1 quanta in sources 2 and 7) are effectively achieved by assigning quanta to a particular fraction of the pixels within a certain region. There is evidence in the mode map for weak source 1 but not source 3. The mode map most closely resembles the  $\Gamma$ -NNLS map from Figure 3d, as expected due to their mathematical similarity. Qualitatively the mode map does a much better job with these data

than the MAXEN algorithm (Figure 3c) and better than the CLEAN algorithm (Figure 3a), considering that the smoothness of the distribution in the CLEAN map is an artifact of the method of cleaning used.

A quantitative comparison of source fluxes derived using the various techniques is given in Table 2. Source fluxes for the CLEAN, MAXEN, and  $\Gamma$ -NNLS techniques are derived by gaussian fits. The CLEAN technique generally recovers at least 70% of the component fluxes, except for the weakest (1 and 3) and most extended (2) sources. The MAXEN technique does the best job of reproducing sizes of strong compact sources, but underestimates the fluxes. The  $\Gamma$ -NNLS technique outperforms both CLEAN and MAXEN for this data set. It recovers a larger fraction of the source fluxes than CLEAN, although fully unconstrained 6 parameter gaussian fits are unstable for weak sources 1 and 3. For the Bayesian mode map, no gaussian fitting is required. All quanta inside or near the half power primary beam radius are clearly assignable to individual sources, except for 3 quanta that might belong to either source 2 or source 5. We empirically assign one of these to source 5 and the remaining two to source 2. The division of flux between these overlapping components is not a proper Bayesian question, or at least is a question which has not been asked here in a Bayesian fashion. Using Gibbs sampling we assign 90% confidence intervals to the source fluxes as described in the next section.

There is one difference in technique used for these flux comparisons which deserves further note. As mentioned above, fluxes for the CLEAN, MAXEN, and  $\Gamma$ -NNLS techniques are derived by gaussian fits. Fluxes for the Bayesian mode map and the Bayesian samples are derived in a manner similar to aperture photometry. An aperture photometry technique would be difficult to implement in an unbiased fashion with CLEAN due to the regions of negative emission surrounding bright sources. That is, calculated source fluxes would often *decrease* with increased aperture size. For MAXEN and  $\Gamma$ -NNLS all residuals are positive, so calculated source fluxes would systematically *increase* with increased aperture size. On the other hand, for Gibbs sampling any source visible in the mean map may have its statistical flux distribution calculated directly from the sampling. Examples are shown in the next section.

### 3.5. Sampling of the posterior density

The details of the Gibbs sampling process are given in Appendix B. Figure 6 shows one run of the Gibbs sampler, starting from the "mode" map of Figure 5. The first few scans increase the number of quanta in the map, reduce  $\chi^2$ , and reduce the posterior. These changes are expected and primarily affect pixels beyond the half-power radius of the main

beam. After about 10 scans a nearly stationary distribution is achieved. This is about the correlation length for the outer pixels, and these first 10 scans (the "burn-in") are discarded. The remaining 200 scans (in this case) produce of order 20 independent realizations of the outer parts of the map. For these high signal-to-noise data and for values of  $q$  this large, the inner pixels are tightly constrained by  $\chi^2$  and are rarely changed in the sampling process. In other words, their coherence lengths are much longer than 200 scans. For smaller values of  $q$ , the coherence lengths for all pixels should be reduced. In the absence of good evidence for mixing of the Gibbs chains, we assume that multiple runs in which the sampler is given different starting points provides an adequate statistical sampling of parameter space. The independence of the various starting points of the sampler depends on the random choice of the quantization level and the probabilistic rounding employed to determine the initial number of quanta in each pixel.

In Figure 7 we show a mean map and a standard deviation map based on 250 independent runs of the Gibbs sampler, each of length 200 scans after burn-in. Except for a few pixels in the highest surface brightness sources, the square-root of the pixel variance is of the same order as, or larger than, the mean flux for that pixel. Such behavior might be expected from examination of the mode map in Figure 5, where the vast majority of the pixels have either zero or one quantum of flux. Figure 7, however, presents only part of the available statistical information, namely the first and second moments of the flux distributions in each pixel. It does not include co-variance information, and there are strong pixel-to-pixel correlations (and anti-correlations). An example is shown in Figure 8.

Due to these strong correlations, Figure 7 by itself does not present enough information to calculate uncertainties in the fluxes of our 8 sources. However, such information is available from the full multi-dimensional probability density. For each scan of each run of the Gibbs sampler, values for the source fluxes are recorded. As with the case of the "mode" map, there is little ambiguity as to which (if any) of the sources a particular quantum belonged, except for the overlapping source 2 and 5. Cumulative probability distributions are shown in Figure 9, and 90% confidence limits are listed in Table 2. In the case of sources 2 and 5, the total flux was attributed 80% to source 2 and 20% to source 5. As discussed earlier, the allocation of flux to one or the other source is not a Bayesian question, since our hypothesis space knows nothing about "gaussians" or indeed even about the existence of discrete "sources".

The actual input source fluxes fall within the 90% confidence limits for 5 of the 8 sources. For two other sources, the true flux lies just above the 90% confidence interval. A tendency to underestimate flux may be due to a cutoff at low  $q$  adopted for practical reasons (Appendix C). Suggestions of emission in several other regions within the half-power beam may be seen in Figure 7. Fluxes have been checked for 3 of these regions (Fig. 9h,i,j) and are consistent

with zero.

## 4. Discussion

### 4.1. Concerns and Cautions

One supposed drawback of methods incorporating maximum entropy is that they underestimate flux densities at peaks in the maps. This indeed appears to be true for MAXEN, for reasons discussed further in Appendix C. This also appears to be true of the Bayesian posterior *mode* map derived here. But the full Bayesian posterior density distribution should not make systematic errors. We show that the Bayesian posterior *mean* map is a much better reflection of the actual photometry. But just as neither the mode, mean, nor median can express the full nature of a general numerical distribution, no single map can represent the entire information contained in the sampled multi-dimensional posterior density.

Another alleged concern with maximum entropy techniques is the variability of the noise and the spatial resolution across the map. This is a true feature of both Bayesian and maximum entropy techniques. Anyone desiring a fixed resolution map may certainly smooth (convolve) a map to produce coarser – but nearly constant – resolution. But such a procedure entails loss of information. It is simply a fact that one can achieve high spatial resolution only with high signal-to-noise ratio.

Some have advocated the use of "data-adaptive models," usually in default image models. A data-adaptive model is essentially a data-adaptive prior. As discussed by Jaynes (2003) and Sivia (1996), this is an incorrect formulation. One must not use a posterior as a prior for a second iteration with the same data. If the "model" is based on information external to the data set being studied, it could be incorporated into a prior. But such a prior may be difficult to formulate exactly. If possible, a preferable course of action would be to treat this external information as real data and incorporate it into the likelihood.

Also remember that we incorporate into our "information" term knowledge about noise statistics, particularly that they are Gaussian. Although Gaussian noise is least informative, noise sources are often non-Gaussian. It may be desirable to incorporate a modified penalty function for large fluctuations, as is often done in robust statistics. Likewise, non-stationary noise would require a more careful treatment.

An optimal imaging algorithm is not a panacea. In fact, it places stronger demands on the observer's knowledge of instrumental characteristics: passbands, telescope pointings, noise levels, beam shapes, etc. The quality of the resulting images can easily be limited by

uncertain knowledge of the true measurement matrix. And the design of an observational program must ensure that the information content of the data is as large as possible, for example by using optimal  $u - v$  coverage.

#### 4.2. Mosaic Imaging

For mosaic imaging, the region of support should be the union of the single dish pointings. In the case of heterogeneous arrays, normally one would preserve the data inside the largest of the relevant combined beams. For dissimilar antenna pairs, the beam is the geometric mean of the individual beams. Otherwise, this technique should easily generalize to handle mosaic data. For modest sized mosaics the number of pixels will grow less rapidly than the number of pointings, due to overlap.

#### 4.3. Error Analysis

At lowest order, error analysis consists of assigning uncertainties (error bars) or confidence intervals to various derived quantities. At a greater level of sophistication one is concerned with the covariance/correlation matrix and with higher moments (higher than second) of the probability distribution. However, to fully understand the uncertainties present in a multi-dimensional distribution one needs to formulate the probability density in any region of parameter space. This cannot be done analytically. But the sampling method described here allows one to approximate this density, to an accuracy limited only by the amount of available computing power. One can then address any well-posed question related to the posterior distribution.

#### 4.4. Self Calibration

Self calibration was discussed briefly in section 2.6. A problem remaining to be solved is the time variation of the complex gains. A common practice is to adopt a self-calibration interval (a time scale for averaging) long enough to provide sufficient signal-to-noise ratio but short enough to allow for correction of atmospheric phase fluctuations. However, these considerations should be formulated into an appropriate prior for the time-dependence of the gains, rather than being based on an *ad hoc* averaging time. The choice of a reference antenna for the phase is also typically made on an *ad hoc* basis. This should be treated objectively, as should the choice between phase-only and phase-and-amplitude correction.

If the signal-to-noise ratio is low, some gains will be poorly known. Treating the complex gains as nuisance parameters is the correct course of action. The problem of atmospheric or ionospheric isoplanicity (Schwab 1984), which arises in wide-field imaging, in principle can also be treated as a Bayesian problem.

#### 4.5. Pixels Redux

There are other possible ways to specify pixelations and basis functions. Although both CLEAN and MEM methods are often described as Fourier inversions, in our development there is no explicit calculation of Fourier coefficients. The visibility data are not gridded in  $u - v$  space, and no advantage is taken of the FFT. The modified Fourier kernel, though, is used to calculate the interferometric likelihood. Pantin & Starck (1996) have proposed an MEM approach utilizing wavelets and a multi-scale measure of entropy. We do not see any clear advantage to their approach, due to the need to enforce non-negativity. We speculate, though, that there may be advantage to adopting other pixelations. Minor gain may be possible with a hexagonal grid of pixels. However, a much greater advantage may be possible by using other pixel sizes or with an adaptive grid approach. A Bayesian approach would tell us how many pixels the data justify and where they should be densest. Small pixels would be used in regions of rapidly-changing brightness with high signal-to-noise, and large pixels would be used elsewhere, such as in the region beyond the half-power beam radius. In the example given above, a reduction in the number of pixels by as much as a factor of 100 may be possible. The posterior would be affected only logarithmically, but the computation time would be greatly reduced.

In all of the preceding discussion we assume that one wishes to produce an image. However, as pointed out by Cornwell, Holdaway, & Uson (1993), "if a scientific question can be answered without making an image, it is best to do so." In such cases the general Bayesian framework should still be used, but a different hypothesis space would be required. The nature of that hypothesis space and the assignment of prior probabilities would depend on the scientific question being addressed. This is why in CMB analysis, images are of secondary interest. For gaussian, isotropic models of the CMB, all cosmologically relevant information is contained in the power spectrum multipole coefficients  $C_l$ .

## 5. Conclusions

We introduce a Bayesian approach to the analysis of radio interferometric data. This approach incorporates the key feature of brightness quantization and a multiplicity prior, differing thereby from conventional maximum entropy techniques. It automatically incorporates Occam’s razor, limiting the amount of detail in the map to that justified by the data. Monte Carlo sampling techniques are used to determine the multi-dimensional posterior density distribution. From this we can determine statistical properties on a pixel-by-pixel basis, such as a mean map, a variance map, and correlations between individual pixels. We can readily deal with heterogeneous arrays, mosaic data, and single-dish data. This technique also has the ability to determine and marginalize over a number of unknown parameters in the measurement matrix. This should allow observers to incorporate self calibration into the map making process in a self consistent fashion. The ability to marginalize over atmospheric or instrumental phase fluctuations may be one of the most valuable aspects of this approach.

This current approach to interferometric imaging arises out of our prior work in a number of different contexts (Sutton et al. 1985, 1995; Wandelt, Larson, & Lakshminarayanan 2003; Wandelt 2004) seemingly unrelated to radio interferometry. This exemplifies, therefore, the growing recognition within the astronomical community of the importance of sophisticated statistical techniques, particularly Bayesian analysis. The range of applicability of such techniques is likely to grow significantly in the near future.

This work was supported in part by the Laboratory for Astronomical Imaging at the University of Illinois, by the National Science Foundation under grants AST 02-28953 and AST 05-07676, by NASA under subcontract JPL1236748, by the National Computational Science Alliance under AST300029N and by the Center for Advanced Studies at the University of Illinois.

### A. Implementation of a Grid Search Algorithm

An appropriate starting point for Bayesian analysis would seem to be an algorithm which is effective at finding good (high) local maxima in the posterior density. This is more difficult than it sounds, due to the discreteness of our configuration space. Finding the global maximum is generally not practical. But we do not need the global maximum. Instead we need a computationally efficient way to find locations in parameter space with high probability which may be used as starting points for the Gibbs sampler. The implementation of the Gibbs sampler itself is given in Appendix B. The algorithm described here was used to

produce the results shown in Figures 4 and 5. Figure 4 was used to estimate optimal values of the quantization level  $q$  and as a way to generate starting points of the individual Gibbs samplers.

Figure 10 illustrates some potential moves in configuration space. We describe a move as *axial* in configuration space if it is a move of unit length along one axis. In other words, it involves a single pixel to which a single quantum is added or, if the pixel is occupied, from which a single quantum is subtracted. A move is *diagonal* in configuration space if single quantum moves are made simultaneously along two configuration axes. In the most common case, such a move is *flux preserving* and also links adjacent pixels. In other words, a quantum is moved from one pixel to one of the eight adjacent pixels in the map. Other moves are more complicated and we use a shorthand in which  $u$  (up) stands for the addition of a quantum and  $d$  (down) stands for the subtraction of a quantum. Our set of additional moves contains  $dd$ ,  $dud$ ,  $duu$ ,  $ddd$ ,  $dudu$ , and  $dududu$ . The moves *axial* and *dd* have no spatial restrictions. For computational practicality, the remaining moves are spatially restricted, generally to sets of pixels with a maximum pairwise separation of three pixels. For fine quantization (small  $q$ ), the simpler moves are generally sufficient. But for coarser quantization, local maxima may be separated by significant distances in configuration space and the more elaborate move set is essential.

Calculation of *diagonal* moves is rapid, due to the limited number of quanta ( $\lambda$ ) present. So searches for *diagonal* moves which make the greatest improvement in the posterior are done frequently. Next most efficient is the search for *axial* moves which make the greatest improvement in the posterior. In configuration space, an *axial* move is a move to a nearest-neighbor on the lattice. A *diagonal* move is a move to a second-nearest neighbor. In a space of large dimensionality, the volume to be searched increases rapidly with the length of the move. Therefore we conduct only very limited searches of third-nearest neighbors and higher.

Other techniques may be more efficient. In particular, problems of this sort are often well suited to treatment by "simulated annealing." For coarse quantization the potential barriers for changing the innermost pixels are large, requiring large pseudo-temperatures to "melt" any initial configuration. Simulated annealing may be an effective technique to explore the vast configuration space available at large  $\lambda$  (small  $q$ ). However, so far we have not found an efficient implementation for small  $\lambda$  (large  $q$ ). As discussed earlier, finding the true maximum of the posterior is not essential. Since a large fraction of the probability lies at moderate  $\lambda$ , a simulated annealing approach may ultimately be most efficient.

## B. Implementation of Gibbs Sampler

A general outline of the Gibbs sampler was given in section 2.5. The first step is to choose an initial value for  $q$  and an initial quantized map. Figure 4 shows that the most probable maps are found with  $q$  equal to about 0.017 Jy/pixel. A naive approach would be to pick  $q$  randomly from a distribution centered on this posterior maximum and with a width determined by the curvature of the log posterior. However, there is a vastly larger volume of configuration space available at larger  $\lambda$  (smaller  $q$ ). The same factor that makes any particular configuration unlikely at small  $q$ , simultaneously says that there will be many more such configurations. To provide an unbiased sampling of the posterior density, we need to start a significant fraction of our Gibbs samplers in this “unlikely” region of parameter space. If the samplers have sufficient mobility, they will automatically cover parameter space in the correct probabilistic sense. However, we have some reason to doubt the mobility of the samplers due to the discreteness (the quantized nature) of the space (see section 3.5) and the high barriers present at large  $q$ . Mobility is somewhat better at small  $q$ . For now we adopt a truncated gaussian distribution in  $q$  with a mean of 0.009 Jy/pixel and a standard deviation of 0.004 Jy/pixel. The truncation rejects values below 0.003 Jy/pixel, a region which is computationally inefficient and also less probable. We do not claim this procedure to be optimal.

Next we need an initial distribution of quanta. We start from our  $\Gamma$ -NNLS map and divide the brightness in each pixel by  $q$ . Then we randomly round fractional pixel values  $n.x$  up to  $n+1$  quanta with probability  $0.x$  and down to  $n$  quanta with probability  $1 - 0.x$ . The search algorithm described in Appendix A is then run until it encounters a local maximum.

From there the Gibbs sampler is started. The conditional probabilities during scan  $j$  to change pixel  $i$  from its current value  $N_i^{j-1}$  to various possible values  $N_i^j$  are proportional to

$$\begin{aligned} \exp[\Delta \text{ posterior}] = \\ \exp[-\Delta\chi^2 + \Gamma(\lambda + 1 + \Delta\lambda) - \Gamma(\lambda + 1) + \Gamma(N_i + 1) - \Gamma(N_i + 1 + \Delta\lambda) - \Delta\lambda \ln n] \end{aligned}$$

where  $n$  is the number of pixels and  $\Delta\lambda = \Delta N_i$ . At each step we accumulate the first and second moments of the probability density of  $\lambda N_i$  based on these *conditional* probability densities. These probabilities are then normalized to add up to unity, and a random draw from  $[0,1]$  is then used to select  $N_i^j$  as that value where the sum of the conditional probabilities exceeds the random number. At the end of each scan we record the values of each pixel and the fluxes within any regions of interest.

At the end of each scan the value of the continuous variable  $q$  is also updated. The curvature of the posterior density with respect to  $q$  may be calculated, suggesting a proposal

density of width

$$q \left( \frac{1}{2} \sum_{k=1}^{N_{vis}} \frac{|V'_k|^2}{\sigma_k^2} \right)^{-1/2}.$$

To encourage  $q$  to sample a larger region of parameter space we double this width. From this a new trial  $q$  is chosen. The remaining details of the sampler are described in section 2.5 and 3.5.

There are undoubtedly more efficient and better mixed types of samplers. The Gibbs sampler has the disadvantage of examining one pixel at a time (equivalent to the *axial* moves described in Appendix A). As we have seen, there can be large potential barriers to the addition or subtraction of individual quanta. Much better would be a Markov chain which implemented *diagonal* moves. One could also envision a sampler which permitted widespread redistributions of existing quanta, as well as additions and subtractions of quanta. So-called genetic algorithms are often recommended for discrete parameter spaces, such as those encountered here. And steps from different procedures may be combined to make a more efficient sampler. Additional programming and testing will be needed to find the best of these possible methods.

### C. Implementation of the $\Gamma$ -NNLS Regularizer

The Gamma function forms the basis of a nearly ideal regularizer for this problem since it is continuous, differentiable, and is exactly equal to the factorials at appropriate integer arguments. However, it has two notable deficiencies. Firstly,  $\Gamma(x + 1)$  is finite for negative  $x$  as long as  $x > -1$ . Such arguments  $x$  correspond to negative brightnesses and are unphysical. Secondly,  $\ln \Gamma(x + 1)$  has a local minimum at  $x = 0.46163$ , which does not correspond to any feature of the physical problem. However, these problems can be solved by some simple modifications.

For our regularizer  $R(x)$  above  $x = 2$  we will use the logarithm of the Gamma function,

$$R(x) = \ln \Gamma(x + 1) \quad x \geq 2.$$

Between one and two we will add the term shown below,

$$\begin{aligned} R(x) &= \ln \Gamma(x + 1) - (\gamma - 1)(x - 1)(x - 2)^3 \\ &= \ln \Gamma(x + 1) - (\gamma - 1)(x^4 - 7x^3 + 18x^2 - 20x + 8) \quad 1 \leq x \leq 2, \end{aligned}$$

where  $\gamma$  is Euler's constant. Between zero and one the regularizer is zero.

$$R(x) = 0 \quad 0 \leq x \leq 1.$$

Negative values of  $x$  encountered in the optimization process are handled by the method of Projection onto Convex Sets (Biemond, Lagendijk, & Mersereau 1990), by setting  $x = 0$ . This regularizer, shown in Figure 11, is continuous, differentiable, and equal to  $\ln x!$  for non-negative integers,  $x$ . It has the additional advantage of being a convex function of  $x$ .

The  $\Gamma$ -NNLS technique is implemented by adopting a penalty function of

$$\frac{\chi^2}{2} + \frac{F}{q} \ln n_{pix} - \ln \Gamma\left(\frac{F}{q} + 1\right) + \sum_i R\left(\frac{f_i}{q}\right)$$

by direct analogy with the Bayesian method, with  $F$  being the total flux,  $f_i$  the flux in the  $i^{th}$  pixel, and  $q$  being the ratio between the flux scale and the arguments of the Gamma functions (thereby playing the same role as the "quantization" level  $q$ , although here we allow continuous values of the flux in each pixel). The ratio  $F/q$  is analogous to  $\lambda$ , the number of quanta in the Bayesian method. The value of  $q$  should be chosen, as in maximum entropy treatments, to give a reasonable value of  $\chi^2$ . For this problem we chose  $q = 0.005$  Jy/pixel, although the result is not very sensitive to this choice of  $q$ . The penalty function is minimized by varying the  $f_i$ . The terms which incorporated Occam's razor in the Bayesian technique here becomes a restriction on the total flux  $F$ , being dominated (for  $F \lesssim q n_{pix}$ ) by the term  $F q^{-1} \ln n_{pix}$ , which penalizes additional flux. This technique converges to the same solution whether starting from a CLEAN component map or a uniform map.

Note the qualitative and quantitative differences between the Gamma function and the entropy function  $x \ln x$  in Figure 11. The logarithm of the leading term in Stirling's formula for  $x!$  is  $\frac{1}{2} \ln(2\pi x) + x \ln x - x$ , which asymptotically approaches  $\Gamma(x + 1)$  for large  $x$ . But at  $x=1$  it gives a value of  $\ln(\sqrt{2\pi}/e) = -0.081$  instead of 0. The term  $-x$  cancels in the calculation of the multiplicity and may be ignored, since  $\lambda = \sum N_i$ . Further ignoring the term  $\frac{1}{2} \ln(2\pi x)$  removes the singularity at  $x=0$ , and leaves the usual form of the entropy function,  $x \ln x$ . The derivative of this entropy function is logarithmically divergent at  $x = 0$ . Therefore maximum entropy techniques will not allow *any* pixel to remain at zero brightness. The entropy function has a minimum of depth  $1/e$  at an argument of  $x = 1/e$ . This is several times deeper than the dip in the Gamma function, and, as noted above, even the dip in the Gamma function has no basis in the physical problem. Unless otherwise constrained by the data, a pixel in a maximum entropy map will seek out a brightness level of  $q/e = F/(e\lambda)$ . The entropy function is narrower and deeper than the Gamma function, indicating that maximum entropy will generally produce overly smoothed maps.

## REFERENCES

Ables, J. G. 1974, A&AS, 15, 383

Armitage, C. & Wandelt, B. D. 2004, Phys. Rev. D, 70, 123007

Bajaja, E. & van Albada, G. D. 1979, A&A, 75, 251

Biemond, J., Lagendijk, R. L., & Mersereau, R. M. 1990, Proc. IEEE, 78, 856

Bracewell, R. N. 1979, ARA&A, 17, 113

Briggs, D. S. 1995, "High Fidelity Deconvolution of Moderately Resolved Sources" (Ph. D. thesis, New Mexico Institute of Mining and Technology)

Brinks, E. & Shane, W. W. 1984, A&AS, 55, 179

Bryan, R. K. & Skilling, J. 1980, MNRAS, 191, 69

Clark, B. G. 1980, A&A, 89, 377

Cornwell, T. J. 1983, A&A, 121, 281

Cornwell, T. J. 1988, A&A, 202, 316

Cornwell, T. J. & Evans, K. F. 1985, A&A, 143, 77

Cornwell, T. J., Holdaway, M. A., & Uson, J. M. 1993, A&A, 271, 697

Cornwell, T. J. & Wilkinson, P. N. 1981, MNRAS, 196, 1067

Ekers, R. D. & Rots, A. H. 1979, ASSL Vol. 76: IAU Colloq. 49: Image Formation from Coherence Functions in Astronomy, 61

Gull, S. F. & Daniell, G. J. 1978, Nature, 272, 686

Gull, S. F. & Skilling, J. 1984, IEE Proceedings, 131 (Pt. F), 646

Hobson, M. P. & McLachlan, C. 2003, MNRAS, 338, 765

Högbom, J. A. 1974, A&AS, 15, 417

Jaynes, E. T. 1982, Proc. IEEE, 70, 939

Jaynes, E. T. 2003, "Probability Theory: the Logic of Science", G. L. Bretthorst, ed.

Mundy, L. G., Cornwell, T. J., Masson, C. R., Scoville, N. Z., Baath, L. B., & Johansson, L. E. B. 1988, ApJ, 325, 382

Narayan, R. & Nityananda, R. 1986, ARA&A, 24, 127

Pantin, E. & Starck, J.-L. 1996, A&AS, 118, 575

Pearson, T. J. & Readhead, A. C. S. 1984, ARA&A, 22, 97

Readhead, A. C. S. & Wilkinson, P. N. 1978, ApJ, 223, 25

Sault, R. J., Staveley-Smith, L., & Brouw, W. N. 1996, A&AS, 120, 375

Schwab, F. R. 1984, AJ, 89, 1076

Schwab, F. R. & Cotton, W. D. 1983, AJ, 88, 688

Shannon, C. E. 1948, Bell System Tech. J., 27, 379

Sivia, D. S. 1996, Data Analysis: a Bayesian Tutorial (Oxford University Press)

Steer, D. G., Dewdney, P. E., & Ito, M. R. 1984, A&A, 137, 159

Sutton, E. C., Blake, G. A., Masson, C. R., & Phillips, T. G. 1985, ApJS, 58, 341

Sutton, E. C., Peng, R., Danchi, W. C., Jaminet, P. A., Sandell, G., & Russell, A. P. G. 1995, ApJS, 97, 455

Thompson, A. R., Moran, J. M., & Swenson, G. W. Jr. 2001, "Interferometry and Synthesis in Radio Astronomy" (2nd ed.) (New York, Wiley)

Vogel, S. N., Wright, M. C. H., Plambeck, R. L., & Welch, W. J. 1984, ApJ, 283, 655

Wakker, B. P. & Schwarz, U. J. 1988, A&A, 200, 312

Wandelt, B. D., Larson, D. L., & Lakshminarayanan, A. 2004, Phys. Rev. D, 80, 083511

Wandelt, B. D. 2004, ArXiv Astrophysics e-prints, astro-ph/0401623

Table 1. Test Object Parameters

Source	Flux (Jy)	$\Delta\alpha$ (arcsec)	$\Delta\delta$ (arcsec)	a (arcsec)	b (arcsec)	pa (degrees)
1	0.105	–20.42	19.09	4.09	3.14	38.07
2	3.772	40.98	35.96	9.37	8.51	36.67
3	0.093	–43.87	10.15	7.36	3.97	69.62
4	0.379	–8.11	–48.52	1.21	0.77	27.07
5	0.718	37.16	21.20	2.76	2.61	–77.24
6	0.177	–13.66	–13.47	2.32	1.35	–69.62
7	0.419	–38.29	–39.88	3.44	3.30	–60.07
8	1.393	24.17	–16.21	1.43	0.79	–56.79

Table 2. Recovered Flux Comparison

Source	Actual Flux (Jy)	CLEAN (Jy)	CLEAN <sup>a</sup> (Jy)	MAXEN (Jy)	Γ-NNLS (Jy)	Bayesian <sup>b</sup> (Jy)	Bayesian <sup>c</sup> (Jy)
1	0.105	0.024	0.029	...	0.101 <sup>d</sup> , 0.044 <sup>e</sup>	0.017	0.013–0.072
2	3.772	0.541	1.001	0.356	2.361	2.203 <sup>f</sup>	2.646–3.189 <sup>f</sup>
3	0.093	...	...	...	0.066 <sup>g</sup>	...	0.011–0.486
4	0.379	0.198	0.330	0.166	0.391	0.376	0.348–0.406
5	0.718	0.347	0.520	0.165	0.666	0.700 <sup>f</sup>	0.662–0.797 <sup>f</sup>
6	0.177	0.117	0.126	0.068	0.178	0.154	0.140–0.193
7	0.419	0.170	0.320	0.133	0.405	0.376	0.332–0.473
8	1.393	1.111	1.328	1.017	1.418	1.366	1.347–1.378

<sup>a</sup>Corrected for primary beam attenuation

<sup>b</sup>Mode map

<sup>c</sup>90% confidence limits in regions of greatest posterior density (i.e. smallest intervals containing 90% of the posterior density). Since this is a Bayesian calculation, these are really *credible* intervals, but astronomers are probably more accustomed to the term *confidence* interval.

<sup>d</sup>Gaussian fit stabilized by fixing major and minor axis lengths.

<sup>e</sup>Flux within 5 arcsec radius

<sup>f</sup>Empirical division of flux between overlapping components

<sup>g</sup>Flux within 10 arcsec radius

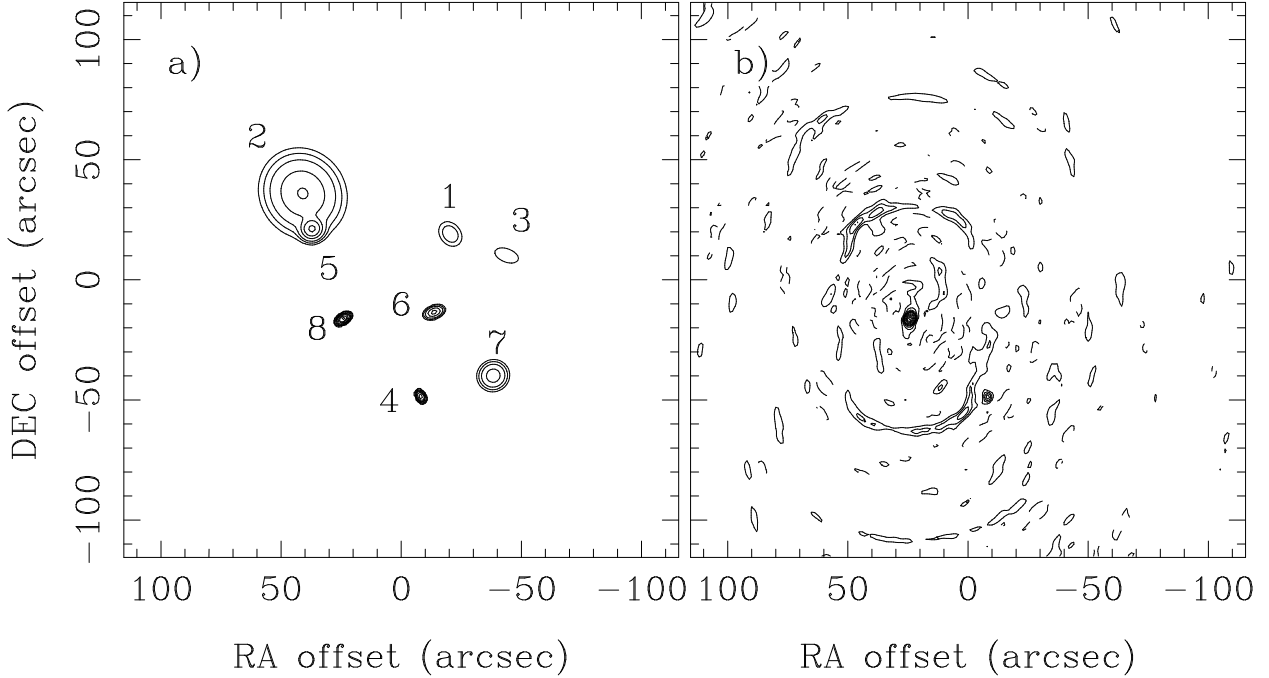


Fig. 1.— a) Test object consisting of 8 elliptical gaussian components. Contour levels are .0005, .001, .002, .005, .01, .02, .05, .1, .2 Jy/pixel. b) Principal solution map with natural weighting. Greatest positive and negative sidelobes of the synthesized beam are +15% and -7%. Largest artifacts in the map are +20% and -12% of peak brightness. Contour levels are multiples of .035 Jy/beam (approximately .004 Jy/pixel). Only sources 4 and 8 are clearly seen in the principal solution (dirty) map.

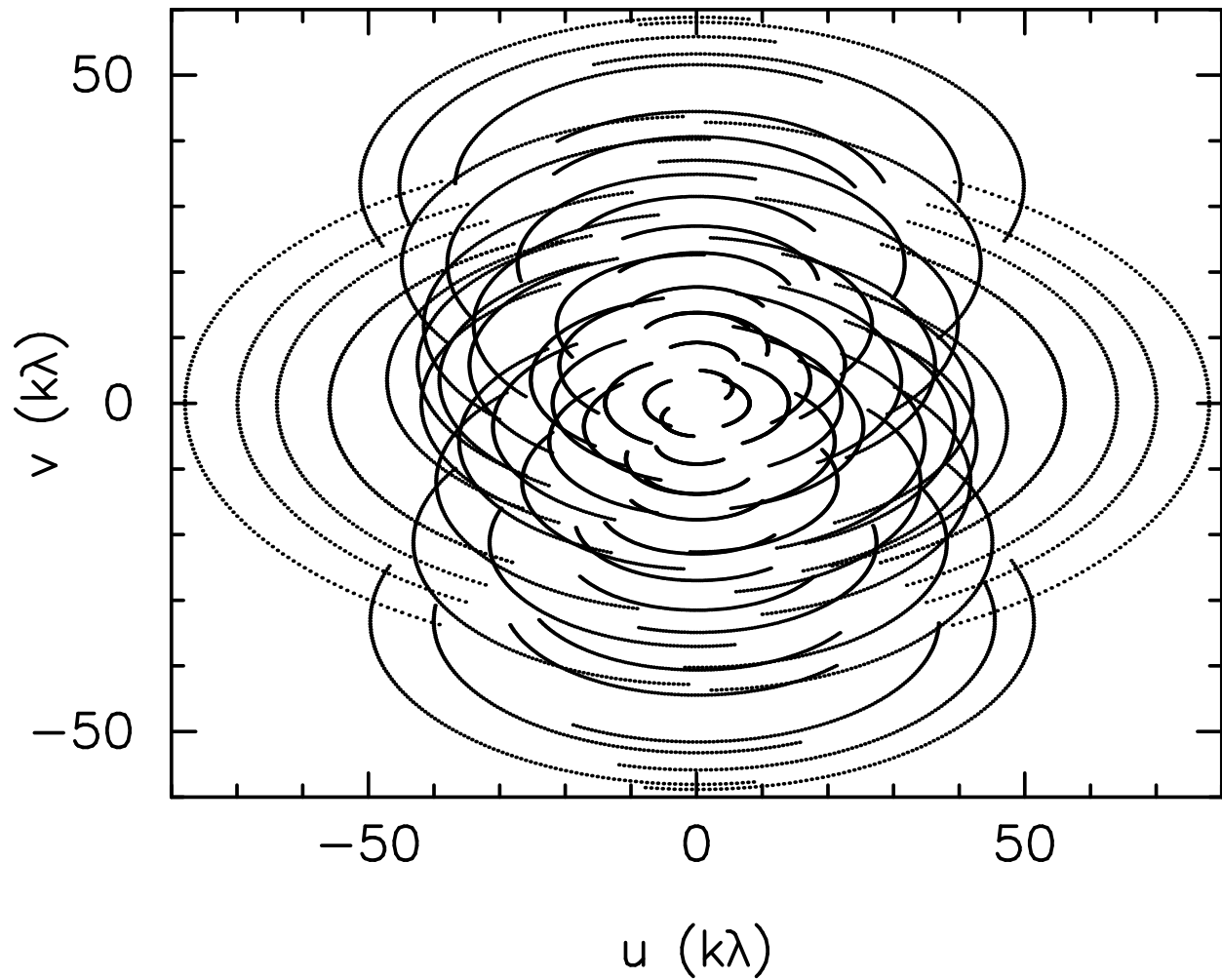


Fig. 2.— Sampling of the Fourier plane in the simulation.

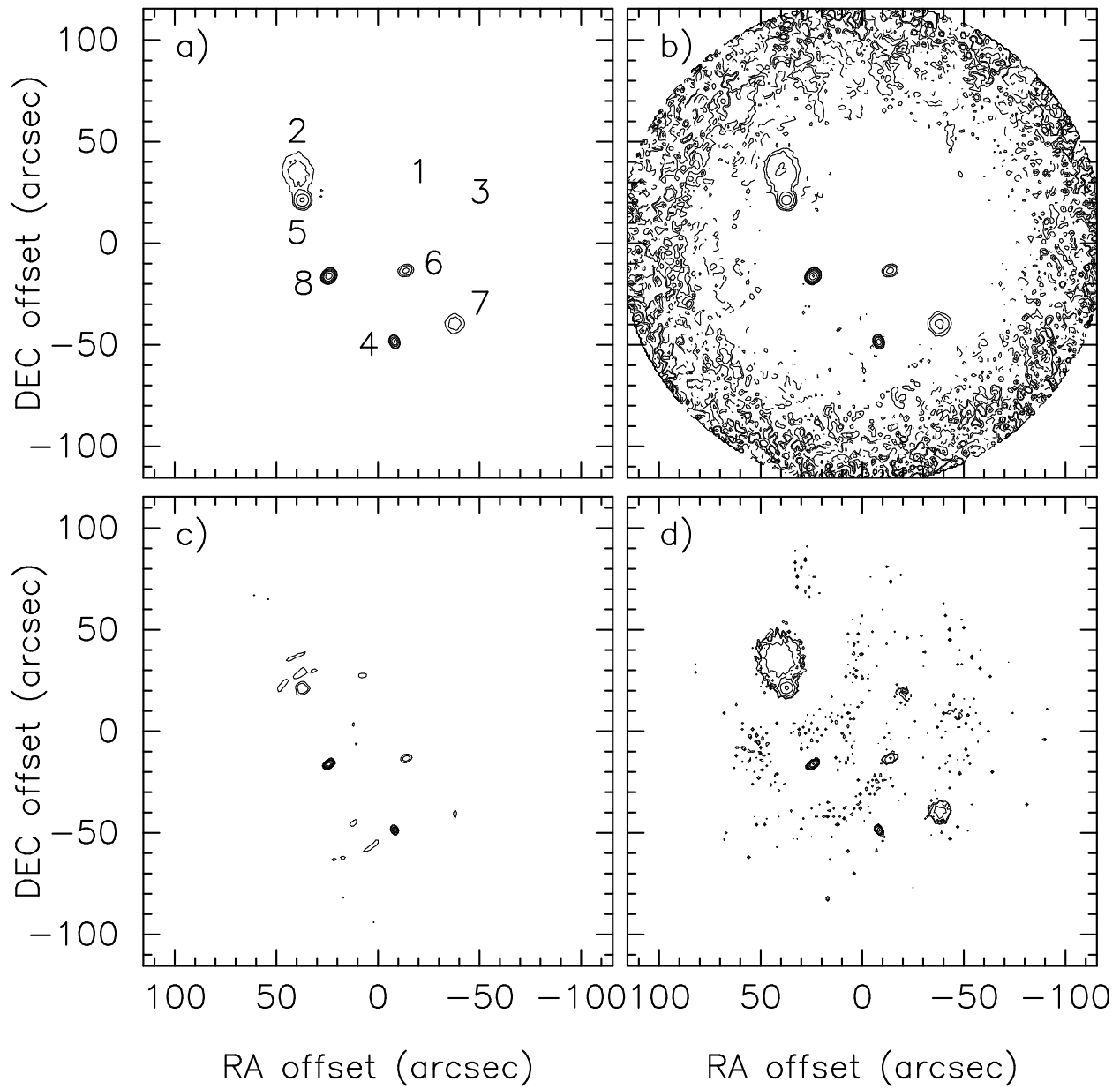


Fig. 3.— a) Map produced by CLEAN algorithm in MIRIAD, restored with a  $2.56 \times 2.07$  arcsec beam. b) Same map produced by CLEAN algorithm, divided by the primary beam in order to correct the photometry. c) Map produced by MAXEN algorithm in MIRIAD. d) The  $\Gamma$ -NNLS map discussed in the text. In all plots the contour levels are .001, .002, .005, .01, .02, .05, .1, and .2 Jy/pixel. Negative contours at the same levels are provided for the CLEAN maps.

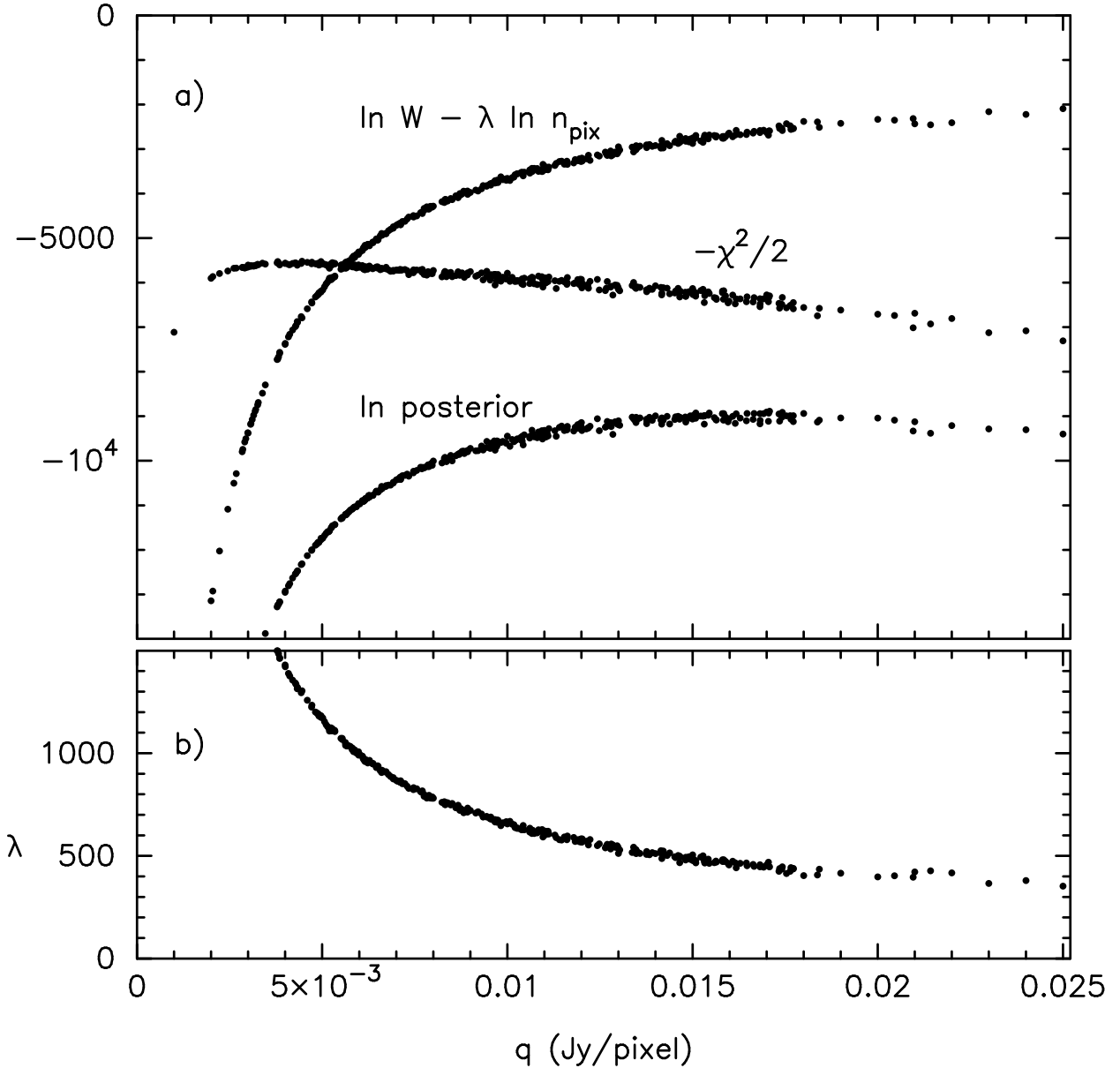


Fig. 4.— a) Variation of the posterior density and the terms  $-\chi^2/2$  and  $\ln W - \lambda \ln n$  with the quantization level  $q$ . b) Optimal number of brightness quanta as a function of the quantization level.

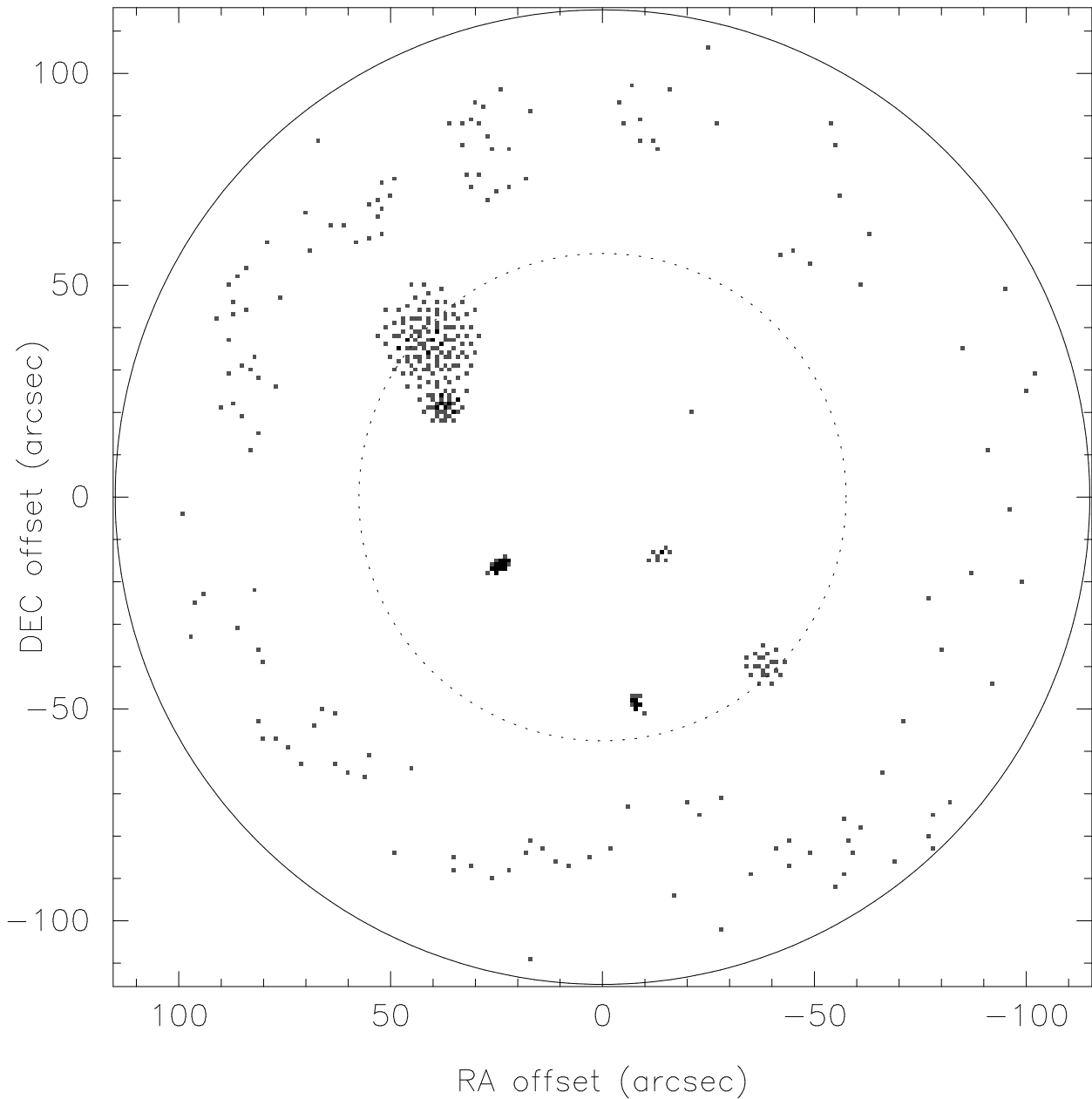


Fig. 5.— Posterior mode map for a quantization level of 0.017 Jy/pixel.

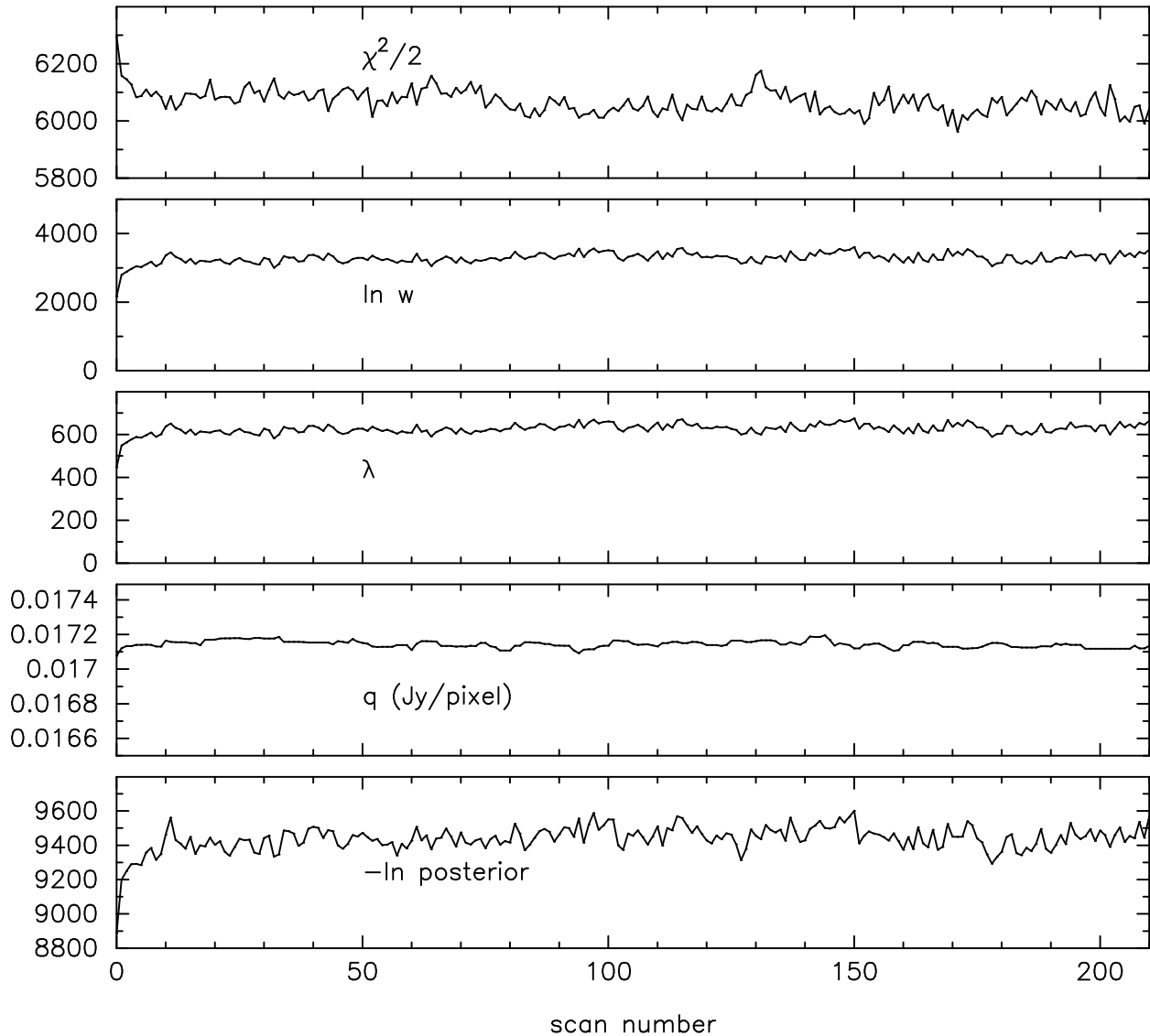


Fig. 6.— Sample run of Gibbs sampler.

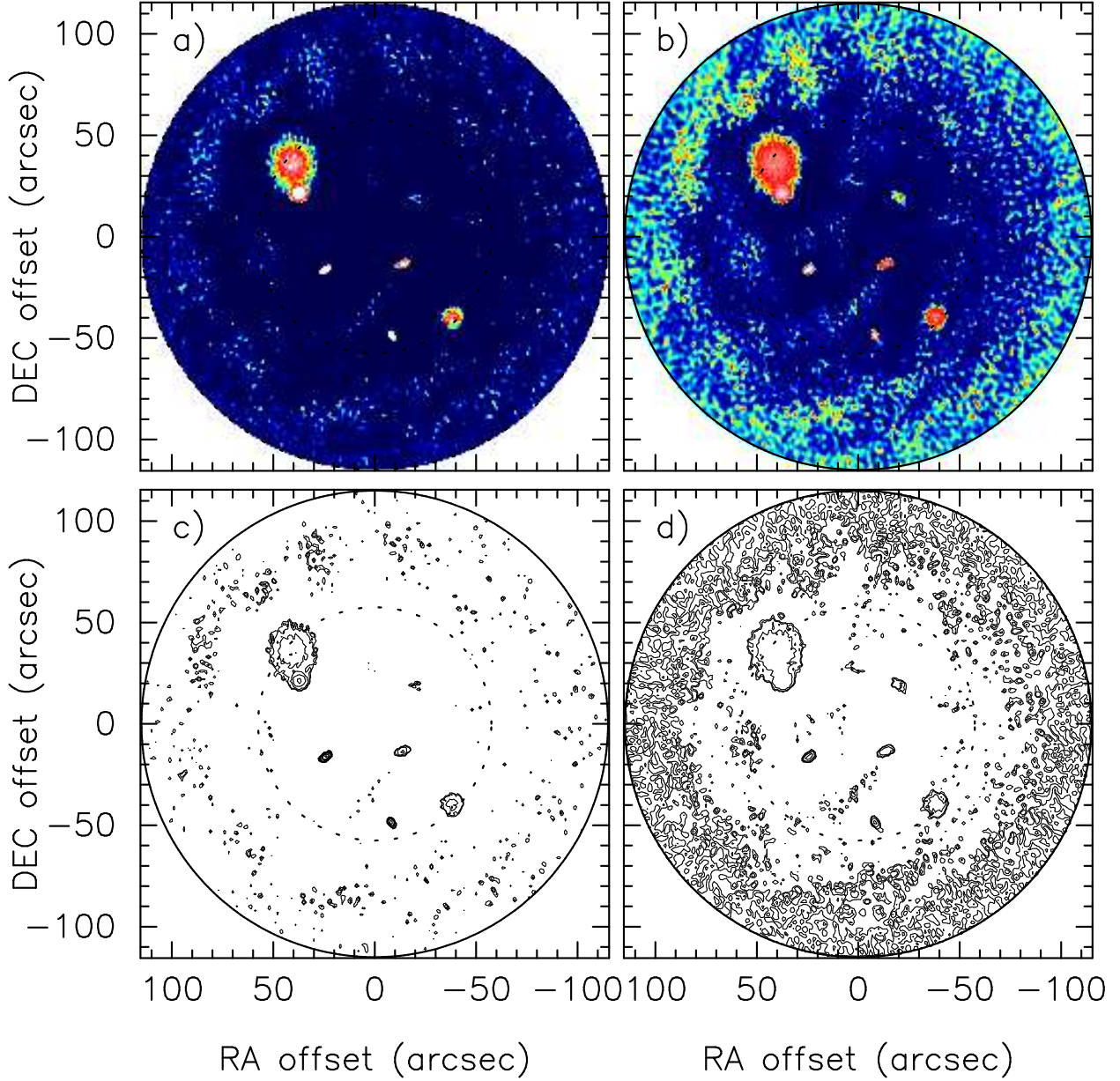


Fig. 7.— Maps based on moments of the pixel by pixel conditional probability density distributions from 250 independent Gibbs samplers of 200 steps each. The mean map is shown in color and contour levels in parts a and c. The standard deviation map in parts b and d uses the same colors and contours as the mean map. The contour levels are .001, .002, .005, .01, .02, .05, .1, and .2 Jy/pixel, the same as for Figure 3. The color scale runs from blue to red (0.005 Jy/pixel) and then saturates on white (0.01 Jy/pixel).

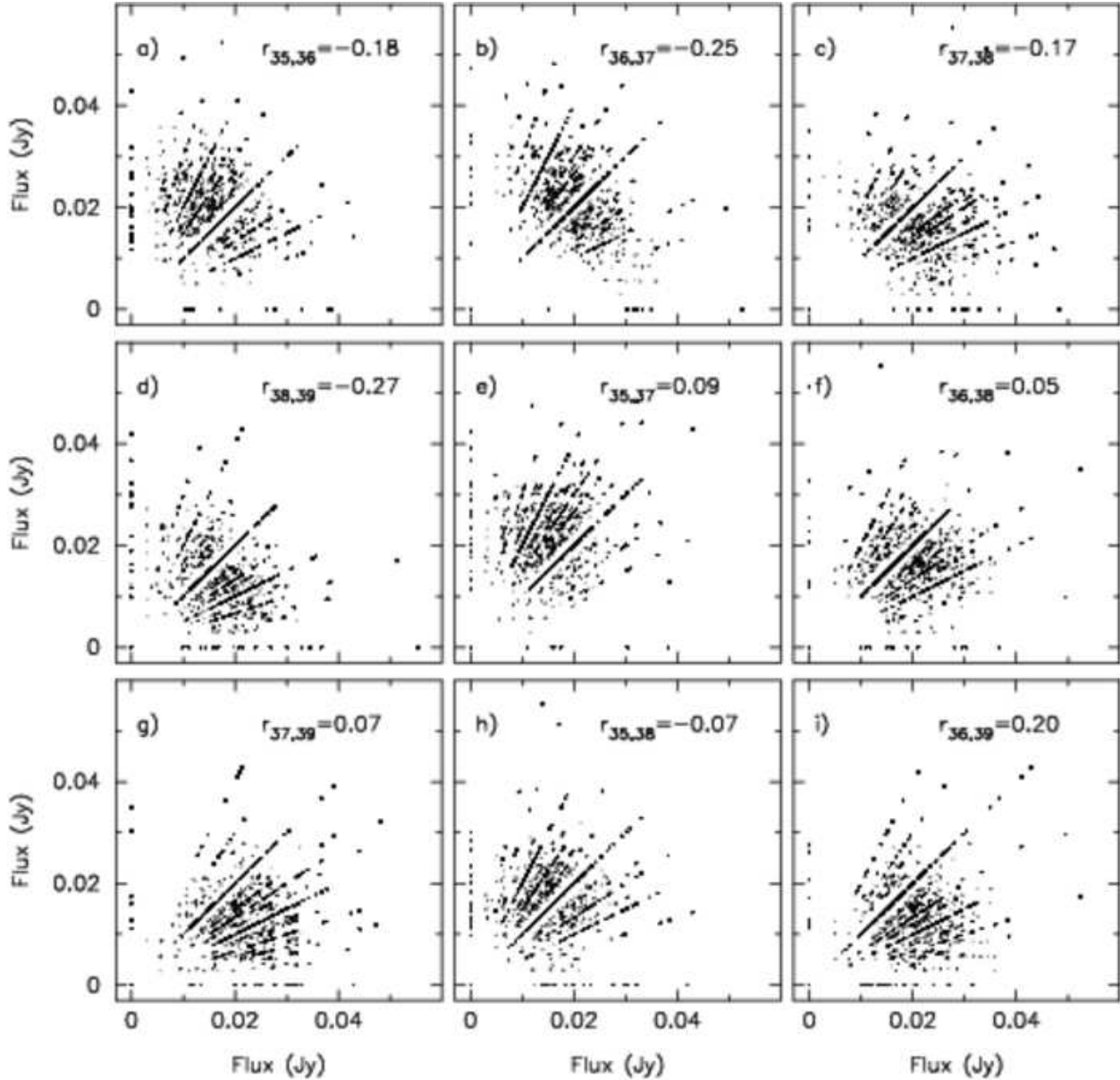


Fig. 8.— Linear correlation coefficients (Pearson's  $r$ ) for pixel pairs on a strip of 5 pixels running across the center of source 5 ( $\Delta\delta = 21, \Delta\alpha = 35, 36, 37, 38, 39$ ). Panels a, b, c, and d show anti-correlations of adjacent pixels. The magnitudes of the correlations are reduced for spacings of 2 arcsec (panels e, f, & g) and 3 arcsec (panels h & i). The diagonal lines in the plots are artifacts of the quantization and have slopes of small integer ratios.

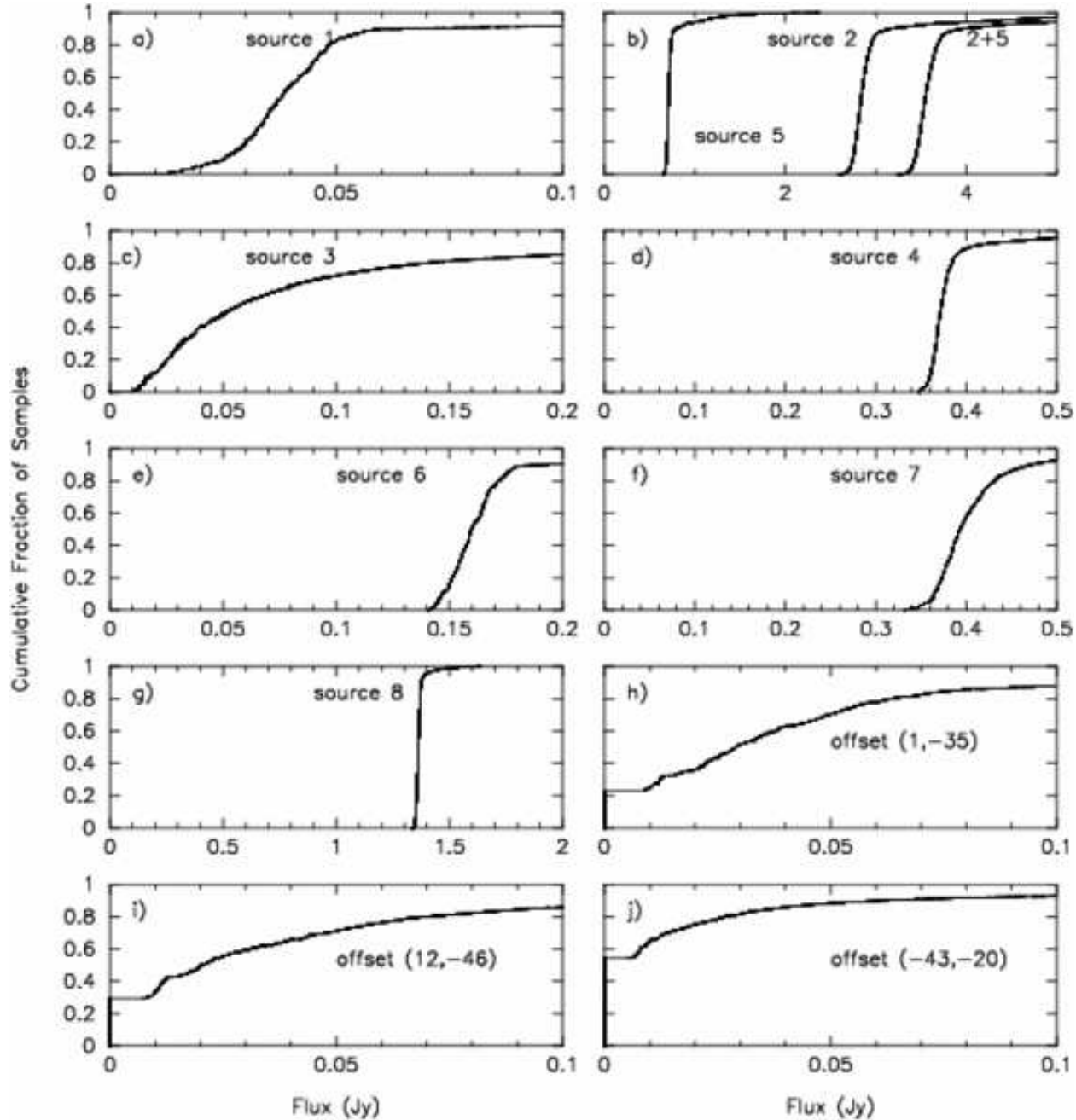


Fig. 9.— Cumulative flux distributions for the eight input sources. Also shown are cumulative distributions for three phantom sources weakly present in Figure 7 at the right ascension and declination offsets shown. These latter distributions are all consistent with zero at the 90% confidence level.

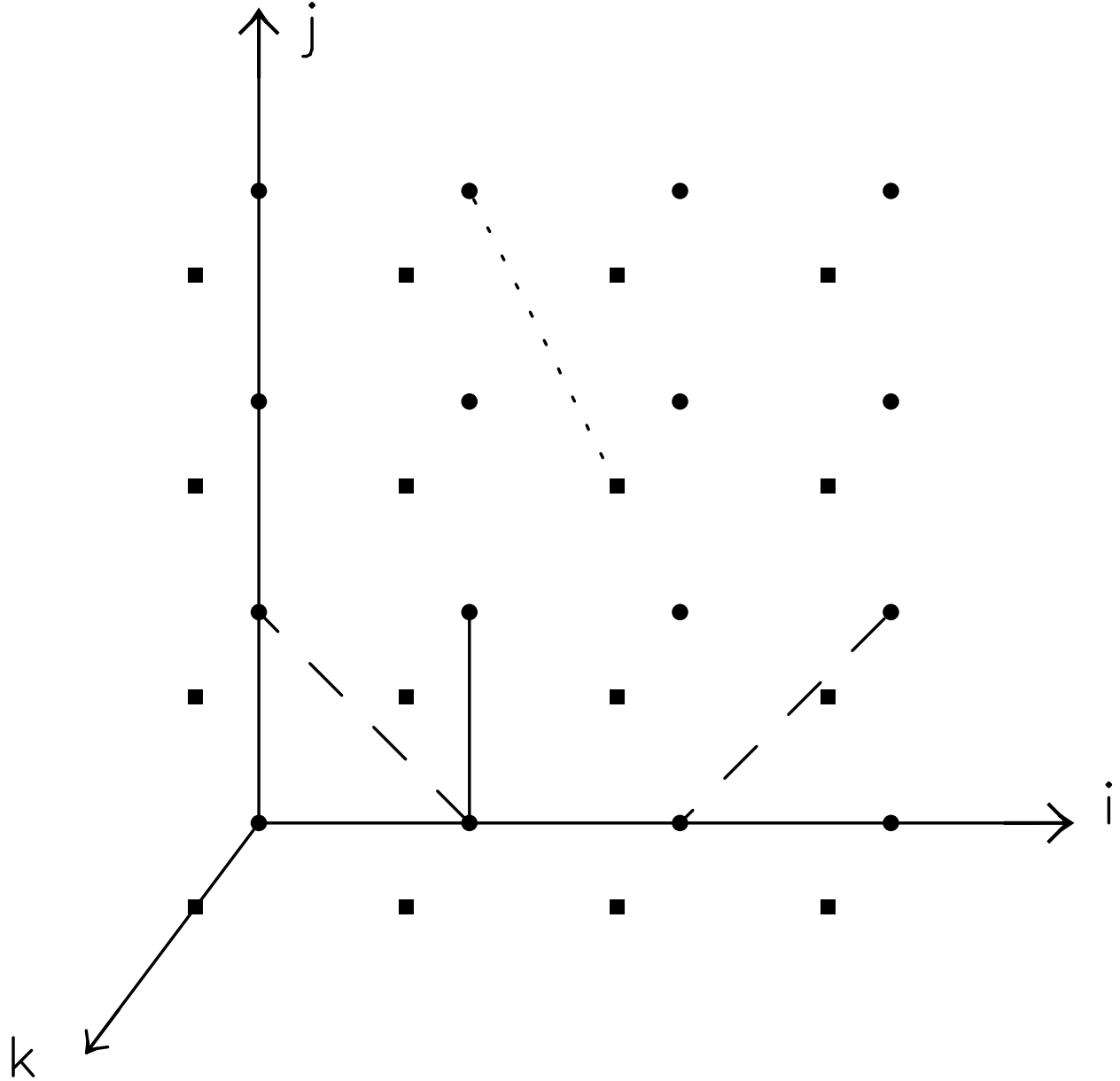


Fig. 10.— Configuration space for representative pixels  $i$ ,  $j$ , and  $k$ . Points represent allowed (quantized) values on the map. Circles indicate the plane  $k=0$  and squares the plane  $k=1$ . Representative moves are shown: "axial" moves of unit length (solid line); "diagonal" moves of length  $\sqrt{2}$  (dashed lines) of both flux conserving (left) and non-flux conserving (right) types; and, as an example of a move coupling 3 or more pixels, a "body diagonal" of length  $\sqrt{3}$  (dotted line).

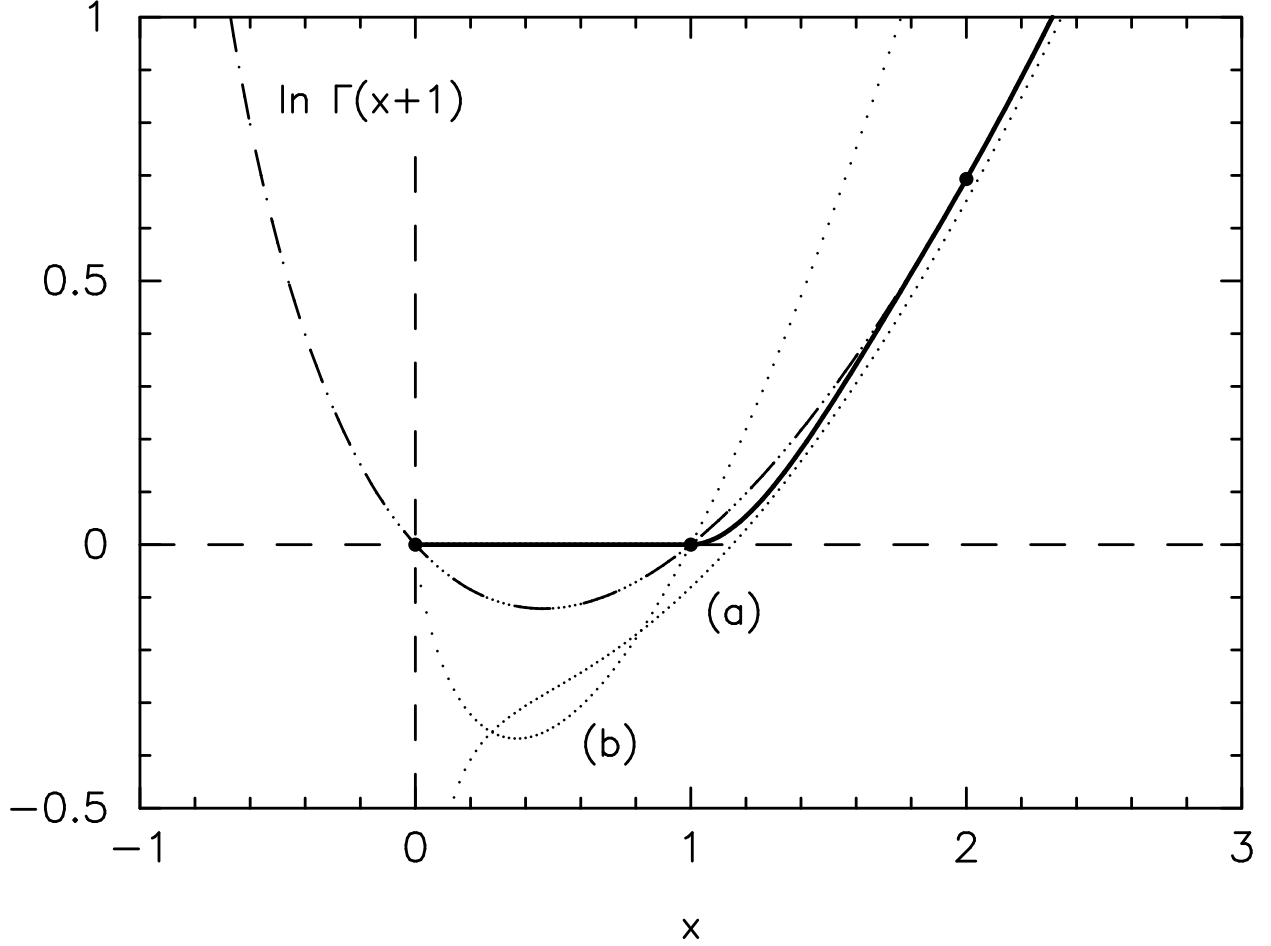


Fig. 11.— Comparison of the regularizer  $R(x)$  (solid bold line) discussed in Appendix C with the logarithm of the Gamma function  $\Gamma(x+1)$  (dot-dashed line). The solid points represent  $\ln x!$  for integer values of  $x$ . Both functions give the correct result at these points. The region  $x < 0$  is unphysical. The dotted lines represent 2 related functions: a)  $\frac{1}{2}\ln(2\pi x) + x \ln x - x$ , the logarithm of the leading term in Stirling's formula for  $x!$ ; b)  $x \ln x$ , the usual form of the configurational entropy (note the minimum at  $x = e^{-1}$  and the logarithmically divergent derivative at  $x = 0$ ).